MOX-Report No. 55/2017

A computational platform for the personalized clinical treatment of glioblastoma multiforme

Agosti, A.; Cattaneo, C.; Giverso, C.; Ambrosi, D.; Ciarletta, P.

MOX, Dipartimento di Matematica
Politecnico di Milano, Via Bonardi 9 - 20133 Milano (Italy)

mox-dmat@polimi.it http://mox.polimi.it

A computational platform for the personalized clinical treatment of glioblastoma multiforme

Abramo Agosti[‡], Clara Cattaneo[‡], Chiara Giverso[♯], Davide Ambrosi[‡], Pasquale Ciarletta[‡]

[‡] MOX– Modellistica e Calcolo Scientifico
Dipartimento di Matematica "F. Brioschi"
Politecnico di Milano
via Bonardi 9, 20133 Milano, Italy
abramo.agosti@polimi.it

[♯] Dipartimento di Scienze Matematiche,
Politecnico di Torino,
Corso Duca degli Abruzzi 24, 10129 Turin, Italy

Keywords: Diffuse–interface model , mixture theory, personalized medicine, finite element, glioblastoma multiforme.

AMS Subject Classification 2010: 35K57, 35K65, 35Q92, 65M60, 92C50.

Abstract

In this work, we develop a computational tool to predict the patient-specific evolution of a highly malignant brain tumour, the *glioblastoma multiforme* (GBM), and its response to therapy. A diffuse-interface mathematical model based on mixture theory is fed by clinical neuroimaging data that provide the anatomical and microstructural characteristics of the patient brain. The model is numerically solved using the finite element method, on the basis of suitable numerical techniques to deal with the resulting Cahn-Hilliard type equation with degenerate mobility and single-well potential. We report the results of simulations performed on the real geometry of a patient brain, proving how the tumour expansion is actually dependent on the local tissue structure. We also report a sensitivity analysis concerning the effects of the different therapeutic strategies employed in the clinical Stupp protocol. The simulated results are in qualitative agreement with the observed evolution of GBM during growth, recurrence and response to treatment. Taken as a proof-of-concept, these results open the way to a novel personalized approach of mathematical tools in clinical oncology.

1 Introduction

Glioblastoma multiforme (GBM) is the most complex and deadliest brain malignancy. Along with the typical hallmarks of cancer (e.g. uncontrolled cellular proliferation, intense resistance to apoptosis, rampant genomic instability [28]), the GBM has a high invasive potential and peculiarly grows along white matter fibers or along vessels, following physical structures in the brain extracellular environment [34, 51]. The resulting diffuse infiltration, as well as the impenetrability of the blood-brain barrier for many conventional drugs, makes the GBM particularly aggressive and difficult to be treated: even after extensive surgery and therapies, the median patient survival does not exceed 10-16 months [33, 34] and the five-years survival rate is around 5% [32, 47]. The currently approved treatment schedule is known as *Stupp protocol* [59]: it involves a surgical removal of the cancerous mass, without injuring eloquent areas and structures of the brain whenever possible, followed by radiotherapy and concurrent and adjuvant chemotherapy. Radiation therapy is used as a treatment because of its precision in targeting the tumour region and its ability to increase the patient survival time, doubling it compared to surgery alone. Since radiotherapy affects both healthy and

tumorous cells, it is performed in various sessions with the intent of maximizing the effect on cancerous cells and simultaneously minimizing the toxicity on normal tissue [52]. In order to obtain the best outcomes with minimal additional toxicity, the Stupp protocol combines the radiation therapy with concurrent chemotherapy, followed by cycles of adjuvant chemotherapy with the cytotoxic agent temozolomide (TMZ) [50, 59].

A key step in order to improve the patient survival rate is the early detection of GBM. Several techniques can be employed for the diagnosis. Nowadays, *magnetic resonance imaging* (MRI) is the technique of election, since it is versatile, noninvasive, harmless and it can provide extraordinarily detailed images of the brain at any location and orientation with sub–millimeter resolution. Although conventional MRI easily permits to identify the functional centers of the brain and the possible location of a brain tumour, it cannot give any insight on the microscopic structure of tissues, e.g. the spatial distribution of the fiber network within the brain. An advance in this direction is given by the *diffusion-weighted magnetic resonance imaging* (DWI), which is a form of MR imaging used to estimate water diffusion within the tissue, so that it indirectly provides some information at a microscopic scale [42]. In some areas of the brain, mostly composed by either grey matter or cerebrospinal fluid, a single scalar diffusion coefficient is sufficient to characterize the diffusion properties, since the measured apparent diffusivity is largely independent on the orientation of the applied gradient (i.e. isotropic diffusivity). On the other hand, in areas where the white matter is dominant, the water mobility is restricted by the tightly packed multiple myelin membranes encompassing the axons, so that the apparent diffusion values strongly depend on the measurement orientation. Addressing this issue, DWI has been developed into a new technique, the *diffusion tensor imaging* (DTI), in which the water diffusivity within each voxel (i.e. a volumetric element) of the brain is described through a tensor. The diagonal elements of the tensor are proportional to the apparent diffusivity along the three main axes, whereas the off-diagonal elements are the covariance terms given by the correlation between molecular displacements in directions perpendicular to the current measurement direction in a given time. The diffusion tensor is symmetric and positive definite, which implies that there are six unknown independent tensor components to be estimated by acquiring at least six DWIs along linearly independent, non-coplanar directions, plus a non-diffusive weighted image giving the reference signal. The DTI technique is nowadays the only non-invasive method for characterizing the micro-structural architecture of the brain bundles and for deriving the preferential direction of water diffusion and, consequently, of cell migration. Indeed it was experimentally proved that glioma cells motion is positively correlated with the white matter fiber tracts, since the tumour cells tend to migrate whilst attached to a solid support [18, 70]. Nonetheless, we remark that DTI does not give a direct measurement of the extent of cell motion and growth along the fiber paths, which is regulated by different chemical and mechanical cues [40, 55].

Mathematical models provide powerful tools to foresee GBM infiltration and progression and foster our understanding on new patient-specific therapeutic strategies. Indeed, in the past few decades, a multitude of increasingly advanced and refined mathematical studies of GBM evolution have been proposed. The models can be gathered into three main categories, depending on the observation scale at which the phenomenon is studied: *discrete models* [13, 39, 44] keep track of the single cell behaviour and its interactions with other agents, updating the system status according to a specific set of biophysical rules; *hybrid models* [16, 25, 26] combine a continuous deterministic model describing the collective evolution of cancer spreading with a discrete model for single cells behaviour and evolution; *continuous models* [10, 14, 27, 33, 63, 64] describe tumour evolution at the tissue macroscopic scale through continuous fields and variables, such as cell densities, volume fractions and biochemical concentrations. The latter class is the most widely used, due to the high number of cells involved in GBM growth and the necessity to describe the tumour evolution at the tissue level in order to obtain clinically meaningful results. In particular, the state-of-the-art focuses on the macroscopic diffusion models of GBM growth developed by Swanson and coworkers [62], which takes into account for a reaction-diffusion equation describing GBM cells concentration. Despite its simplicity, this Proliferation-Infiltration (PI) model can account for the augmented tumour motility in white matter as compared with grey matter thanks to either a heterogeneous diffusion coefficient (i.e. a piecewise-function with two different constant values for grey and white matter) [62, 63], or the definition of an anisotropic and heterogeneous diffusion tensor [37] directly computed from DTI images. Nevertheless, these models [37, 62, 63] do not provide insights on the chemical and mechanical cues that drive cell motion along fibers tracks, lacking a mechanistic connection between water diffusion, brain geometry and tumour cell invasion. Some efforts in this direction have been done in [22, 48, 61], where an anisotropic diffusion equation [48, 61] or an advection-diffusion model [22] for GBM invasion have been derived through the parabolic scaling limit of mesoscopic transport equations, and by defining a systematic approach for

connecting DTI data to parameters in the macroscopic model, through a bimodal von Mises-Fisher distribution [48]. However, all these models [22, 37, 48, 61–63] neglect the generation and accumulation of forces between the host and the malignant tissue and the mechanical interactions occurring within the tumour itself, which should be incorporated in a continuous mechanical model.

In particular, *multiphase models* [3], based on the theory of mixtures [8], represent a natural modelling framework for studying GBM evolution (and, more generally, solid tumour growth) at a macroscopic scale. Indeed, they allow taking into account mechanical and biochemical interactions among multiple solid cell species and extra- or intracellular liquids [3, 11, 17, 69]. Multiphase models consider the tumour as a saturated medium, comprising at least one solid phase (e.g. cells, extracellular matrix, etc) and one liquid phase (e.g. water), and incorporate mass, momentum and energy balances to describe the evolution of the system. A first attempt to study GBM evolution with a multi–phase model is found in Colombo et al. [15], where clinical neuroimaging patient-specific data have been combined with a continuous multiphase mechanical model. Specifically, the mass and momentum balance laws of a binary mixture composed by tumour cells and healthy environment lead are coupled with a reaction-diffusion equation for the nutrients, guiding the proliferation and the motion of tumour cells.

In this work, we extend the model proposed in [15] by introducing an anisotropic description of the dissipative and conservative interactions between the phases and we provide a more accurate calculation of the tensor of preferential directions accounting for the local orientation of the fiber network. Furthermore, we take into account for the tumour response to the standard therapeutic treatment [58]. The proposed mechanical model introduces nontrivial differences with respect to the state-of-the-art PI model and the standard examples found in the literature [1]. In particular, in the present model the resulting degenerate Cahn-Hilliard type equation, describing the tumour phase dynamics, introduces some analytical and numerical difficulties, such as non-uniqueness of the solution and presence of solutions with unphysical behaviour [6], which must be properly addressed in order to select the physically meaningful solution and to avoid the onset of numerical instabilities. Moreover, a naive discretization of the model would lead to discrete solutions which do not respect the positivity property of the corresponding continuous solution [5]. Following and extending the analysis introduced in [1], the present model is conveniently discretized in order to select the physical viable solution, and the positivity property on the discrete solution is imposed as a constraint through a variational inequality.

The paper is structured as follows. In section 2 the mathematical model of a GBM growth is introduced. In section 3 we describe how the numerical model and the patient-specific data have been obtained from the MRI and DTI images, kindly provided by the *Istituto Neurologico Carlo Besta* (Milan , Italy), and we present the discretized model and the numerical algorithm used to solve it. Finally, the numerical results are illustrated and discussed in section 4.

2 Mathematical model

In this section we derive a continuum multiphase diffuse-interface model [3] of GBM accounting both for its growth (section 2.1) and its response to therapies, according to the standard Stupp protocol, (in order to study cancer recurrence (section 2.2)). The biological range of the model parameters is discussed in section 2.3.

2.1 GBM growth model

Following [11, 12, 15], we represent the tumour as a binary, saturated, closed mixture of incompressible constituents, which is composed by a *cellular* phase of proliferating tumour cells, with volume fraction ϕ_{c}, and a *liquid* phase, with volume fraction ϕ_ℓ, resuming hosts cells, nutrient, water and interstitial fluid. We do not distinguish between dead and viable tumour cells, the former being considered to belong to the liquid phase. We denote by $\boldsymbol{v}_i(\mathbf{x}, t)$, $i = \{c, \ell\}$, the convective velocity of each phase; the *true mass densities* [8] of each species is constant and equal to the water density γ (since the cells are mostly composed by water), and the mass balance for each phases reads

$$\frac{\partial \phi_i}{\partial t} + \nabla \cdot (\phi_i \boldsymbol{v}_i) = \frac{\Gamma_i}{\gamma} + \nabla \cdot \boldsymbol{k}_i \tag{1}$$

where $i = \{c, \ell\}$. Here, Γ_i represents the volumetric mass production (respectively loss) of the corresponding phase, $\boldsymbol{k}_i$ is the non-convective mass flux of the i-th phase. Being the mixture closed, $\Gamma_{\mathrm{c}} = -\Gamma_\ell$ and $\boldsymbol{k}_c = -\boldsymbol{k}_\ell$ in order for

the mixture to locally satisfy the conservation of mass and fluxes exchanged between the phases.

The growth-loss and the mass flux are modulated by the local concentration of nutrients and possibly other chemicals (e.g. growth factors). Here, we consider oxygen as the main nutrient for tumour cells and we define $n(\mathbf{x}, t)$ as the dimensionless concentration of the diffusing nutrient, normalised with respect to the typical physiological concentration n_s of nutrient in the capillaries. For simplicity, in the following, ϕ_c will be replaced by ϕ. Now, we set

$$\Gamma_c = \nu\gamma[n-\delta]_+\phi(1-\phi) - \nu_d\gamma[\delta-n]_+\phi - R(\phi,t) - G(\phi,t)\,, \tag{2}$$

where $[\cdot]_+$ stands for the positive part of its argument, ν and ν_d are the neoplastic cells proliferation and death rates respectively and δ is a threshold value for hypoxia. According to the functional form (2), the cells proliferate as long as the nutrient concentration is above δ times n_s and the saturation state is not reached (contact inhibition); in hypoxia conditions ($n < \delta$) the rate of apoptosis prevails over the mitosic rate and Γ_c is negative. The loss terms $R(\phi, t)$ and $G(\phi, t)$, whose form is to be detailed in section 2.2, represent cell death due to radiotherapy and chemotherapy, respectively.

The non-convective mass flux describing the chemotactic motion of cells is proportional to the nutrient gradient [15]

$$\boldsymbol{k}_c = -k_n\phi n_s \boldsymbol{T}\nabla n\,. \tag{3}$$

Here, k_n is a specific chemotactic parameter and $\boldsymbol{T}$ is a positive definite symmetric tensor defining the preferential directions of the chemotactic movement, obtained from Diffusion Tensor Imaging measurements, (which is a modification of the standard equation used to model chemotaxis [17, 29, 35] to take into account the preferential motion of cells along fibers). Thereby, the term $\boldsymbol{k}_c$ is able to describe the tendency of tumour cells to direct their movements uphill the gradient of nutrients. Note that $\boldsymbol{T}$, being a positive definite symmetric tensor, does not contain a rotating component.

In order to close the equations system, we derive the constitutive laws for $\boldsymbol{v}_i$, following the thermodynamically consistent approach proposed by Doi and Onuki [19] and defining an energy formulation of viscous interactions and mechanical forces involved in cell-cell and cell-matrix (ECM) adhesion. Differently from [15], we assume that the viscous interactions due to the relative motion between the cells and the healthy phase, which are the main source of energy dissipation in the system, have the following anisotropic distribution

$$W = \frac{1}{2}\int_\Omega \phi(\boldsymbol{v}_c - \boldsymbol{v}_l)^T \boldsymbol{M}(\boldsymbol{v}_c - \boldsymbol{v}_l)d\Omega\,, \tag{4}$$

where $\boldsymbol{M} = M_0\boldsymbol{T}^{-1}$, and M_0 is a friction parameter. According to energy dissipation (4), the directions of higher diffusion of water molecules, captured by DTI and encoded in the largest eigenvalues of the tensor $\boldsymbol{T}$, are also the ones most easily accessed by the cells in their motion. Here $\Omega \subset \mathbb{R}^3$ is the fixed spatial domain occupied by the mixture at any time instant and coinciding, in our case, with the whole brain of the patient, which remains unchanged while the tumour evolves. The introduction of tensor $\boldsymbol{T}$ to account for non-isotropic dissipative and mechanical interactions inside the mixture is an innovative aspect of this work, in order to mimic the preferential motion of cells along white matter fiber tracts [31, 37, 39], whose orientation can be inferred by the diffusion tensor. The Helmholtz free energy of the system takes into account both the local interactions among cells *within* each phase and the interactions *between* the two phases:

$$F = \int_\Omega \left(\psi(\phi) + \frac{\epsilon^2}{2}|\nabla\phi|^2\right)d\Omega\,. \tag{5}$$

The first term $\psi(\phi)$ is the free energy per unit volume due to cell-cell and cell-matrix adhesion of the two phases, whereas the second term represents the non-local intermixing and adhesion forces that generate a surface tension between the tumour and the host tissue, across a diffuse interface of thickness proportional to the value of ϵ. According to [19], the minimization of the Rayleighian $\mathcal{R} = W + dF/dt$ with respect to $\boldsymbol{v}_c$ and $\boldsymbol{v}_l$ after the introduction of a Lagrange multiplier in order to account for the incompressibility constraint of the mixture lead to the following relation for the relative velocities of the two phases:

$$\boldsymbol{v}_c - \boldsymbol{v}_l = -\left(\frac{1-\phi}{M_0}\right)\boldsymbol{T}\nabla\left(\frac{\partial\psi}{\partial\phi} - \epsilon^2\Delta\phi\right). \tag{6}$$

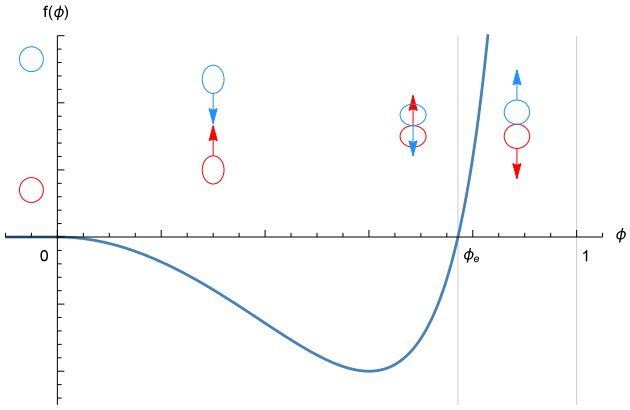

Figure 1: When two cells (here represented with blue and red circles) are sufficiently far from each other, they do not interact; as soon as the distance between them falls below a certain value, e.g. because of an increase in density, they are affected by the closeness and experience attractive forces (red and blue arrows) until they come in contact ($f(\phi) < 0$); if the cell volume fraction ϕ goes beyond the equilibrium value ϕ_e, the forces become repulsive ($f(\phi) > 0$) and tend towards infinity as $\phi \longrightarrow 1$, i.e. when cells fill the whole volume. Image adapted from [11].

In the absence of external forces and considering a high viscosity for the mixture, the center of mass of the mixture does not move, so that (6) reduces to a Darcy-like law for the velocity of the cell phase:

$$\boldsymbol{v}_c = -\boldsymbol{K}(\phi)\nabla\Sigma\,. \tag{7}$$

where

$$\boldsymbol{K}(\phi) := \frac{(1-\phi)^2}{M_0}\boldsymbol{T}, \tag{8a}$$

$$\Sigma := \frac{\partial\psi}{\partial\phi} - \epsilon^2\Delta\phi = f(\phi) - \epsilon^2\Delta\phi\,. \tag{8b}$$

$\boldsymbol{K}(\phi)$ is a motility tensor depending on the cells volume fraction and motion preferential directions, whereas Σ is the excess of pressure exerted by the cells. Cell-cell interactions are expected to be attractive at a moderate cell volume fraction and repulsive at higher densities. Hence it exists a threshold value ϕ_e, called *state of equilibrium* or *undeformed state*, corresponding to which no action is exerted on the neighbours, i.e. $f(\phi_e) = 0$. For $\phi < \phi_e$ cells are attracted to each other and $f(\phi) < 0$, while for $\phi > \phi_e$ cells experience a repulsive force and $f(\phi) > 0$ [11]. In order to obey to the observed physical and biological behaviours, instead of a double-well potential, usually employed in phase transformations [69], we use a phenomenological form of $f(\phi)$ (Fig. 1) as in [3, 11, 12], i.e. a single-well Lennard-Jones type potential:

$$f(\phi) = E\frac{\phi^2(\phi-\phi_e)}{1-\phi}, \qquad \phi > 0\,, \tag{9}$$

where E is the Young modulus of the cancerous phase [11].

Lastly, we have to represent the evolution of the nutrient concentration n inside the brain. We assume that the vasculature is homogeneous in the whole domain and no angiogenesis occurs. Nutrients are released from the vasculature at a rate S_n as long as $n < 1$, while they are back absorbed by the vasculature when $n > 1$. The nutrients supply is also slowed down by the proliferation of the tumorous cells destroying blood vessels. Then the released oxygen diffuses into the interstitial fluid as described by the diffusion tensor $\boldsymbol{D}$ and is eventually consumed by the neoplastic cells at a constant rate δ_n, whereas the net nutrient uptake by the host tissue is negligible since all the oxygen absorbed by the healthy cells is instantaneously replaced by the vasculature.

Therefore, the complete system of equations representing GBM growth reads:

$$\begin{aligned}\frac{\partial \phi}{\partial t} &= \nabla \cdot \left(\frac{\phi(1-\phi)^2}{M_0} \boldsymbol{T} \nabla (f(\phi) - \epsilon^2 \Delta \phi) \right) + \nu \phi [n-\delta]_+ (1-\phi) - \nu_d \phi [\delta - n]_+ \\ &\quad - \nabla \cdot (k_n \phi n_s \boldsymbol{T} \nabla n) - R(\phi, t) - G(\phi, t)\,, \end{aligned} \tag{10a}$$

$$\frac{\partial n}{\partial t} = \nabla \cdot (\boldsymbol{D} \nabla n) + S_n (1-n)(1-\phi) - \delta_n \phi n\,. \tag{10b}$$

with proper initial and boundary conditions (see section 4.2). We note that equation (10a) is a degenerate Cahn-Hilliard type equation with a single well potential and source terms.

2.2 Modeling the therapy effects

In this section, we detail the modeling of the clinical therapy, consisting of surgical resection followed by external beam radiation therapy (RT) and chemotherapy (CHT), according to the standard Stupp protocol. Radiotherapy consists of fractionated focal irradiation at a dose of 2 Gy per fraction (1 Gy = 1 J/kg) given once daily, five days per week (Monday through Friday) over a period of six weeks, for a total dose of 60 Gy. Concomitant chemotherapy consists of TMZ at a dose of 75 mg/m^2 per day, given 7 days per week from the first to the last day of radiotherapy. After a 4-weeks break, patients receive up to six cycles of adjuvant TMZ according to the standard 5-day schedule, every 28 days. The dose is 150 mg/m^2 for the first cycle and is increased to 200 mg/m^2 for the remaining cycles [58] (see Fig. 2).

The loss terms $R(\phi, t)$ and $G(\phi, t)$ in (10), representing cell death due to radiotherapy and chemotherapy respectively, are considered to be proportional to the tumour population, as in [50]:

$$R(\phi, t) = k_R(t)\phi, \qquad G(\phi, t) = k_C(t)\phi. \tag{11}$$

We assume that they have different toxicity profiles (toxicity independence) [59], hence they can both be added to the first equation of the system (10). The functions $k_R(t)$ and $k_C(t)$ are the temporal profiles of the therapies schedules: they are zero on rest days, when no therapy is provided, while they are equal to the cell death rate due to the administration of radiation or drug on treatment days. Therefore, they are represented by the following piecewise constant functions:

$$k_R(t) = \begin{cases} R_{eff} & t_i \le t \le t_{i+1} \\ 0 & \text{otherwise} \end{cases} \qquad k_C(t) = \begin{cases} k_{C1} & s_0 \le t \le s_1 \\ k_{C2} & s_2 \le t \le s_3 \\ k_{C3} & s_j \le t \le s_{j+1} \\ 0 & \text{otherwise} \end{cases} \tag{12}$$

where the coefficients k_{C1}, k_{C2} and k_{C3} are estimated from clinical data and reflect the increasing drug dosage (75 mg/m^2, 150 mg/m^2 and 200 mg/m^2 respectively), while t_i with $i = 0, ..., 10$ are, alternately, the days at the beginning and at the end of radiotherapy administration periods and s_j with $j = 4, ..., 12$ are, alternately, the days at the beginning and at the end of chemotherapy administration cycles ($t_0 = s_0$), according to the standard Stupp protocol (see Fig. 2).

On the other hand, the radiotherapy death rate R_{eff} is modelled via the linear-quadratic (LQ) model, which is the best description model for the radiation induced damage in the clinically relevant low-dose region (0-3 Gy) [68]. Assuming that the irradiation duration of the single fraction per day is very short, R_{eff} remains constant throughout the entire period of the treatment and the radiotherapy death rate can be expressed by:

$$R_{eff} = \alpha m d + \beta m d^2\,, \tag{13}$$

where d [Gy] is the dose of radiation for every fraction, m is the number of fractions per day (here, $n = 1$ day^{-1}), α [Gy^{-1}] and β [Gy^{-2}] are two tissue-dependent parameters, called respectively the *linear* and *quadratic* coefficients for cell kill [52, 54]. We remark that the LQ model takes into account both *lethal* lesions (i.e. when a single ionizing particle provokes a double-strand break in DNA) and *sublethal* lesions (i.e. a single-strand break in DNA that may be repaired if no further damage occurs): the linear term αd in (13) is related to double-strand breaks, whereas the term βd^2 accounts for the misrepair of repairable damage, which gives rise to superlinear effects. The dose at which

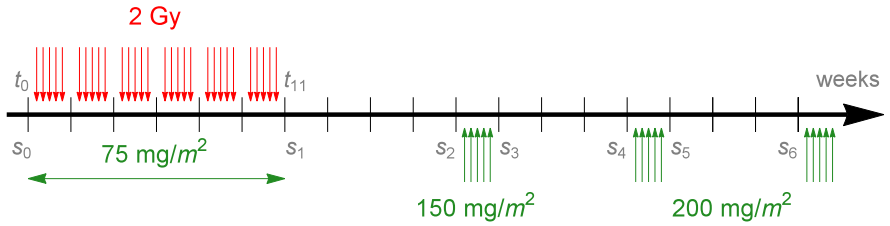

Figure 2: The standard Stupp protocol: RT (in red) at 2 Gy/day five days per week, for six weeks; concomitant CHT (in green) with TMZ at a daily dose of 75 mg/m^2 from beginning until ending of RT; six cycles of adjuvant CHT at a dose of 150 mg/m^2 (only first cycle) and 200 mg/m^2 (remaining cycles). Image adapted from [50].

the contributions from the first and second term, i.e. the probability αd of lethal damages and the probability βd^2 of misrepaired sublethal ionizing events, are equal is given by α/β [Gy], generally called the *alpha-beta ratio*. This parameter is an inverse measure of a tissue's sensitivity to fractionation, i.e. the size of dose given on each treatment, distinguishing late responding tissues, with low alpha-beta ratios ($\alpha/\beta \simeq 2$ Gy), and early responding tissues, with high alpha-beta ratios ($\alpha/\beta \simeq 10$ Gy) [24, 46].

2.3 Parameters estimation

A mathematical model is clinically useful and potentially predictive only if its parameters can be measured from specific and, possibly, patient-specific biological experiments. In principle, each parameter appearing in (10) can be estimated from in-vitro and in-vivo biological tests or directly extracted from clinical exams; as an example $\boldsymbol{D}$ and $\boldsymbol{T}$ can be obtained from patient-specific DTI images (see section 3.1). A comprehensive list of reference values for the introduced parameters and the corresponding source is reported in Table 1. In this section, we discuss the parameters whose derivation from the literature is not straightforward.

According to [36], M_0 can be estimated as the inverse of the hydraulic conductivity found in [60]. The equilibrium cell volume fraction ϕ_e can be estimated as the complementary value of the extra–cellular space (ECS) studied in [9], which is composed of vascular and interstitial space. Moreover, ϵ can be inferred by the characteristic distance for cells interaction $\epsilon/\sqrt{\chi}$, which is considered to be equal to the cell size (with radius r). Here, we interpret the characteristic pressure χ as the interstitial fluid pressure (IFP) [7]: it has been proven that the fluid flowing in the interstitial compartment, which is the space between blood vessels walls and cellular membranes, exerts a different pressure depending on the tissue being healthy or neoplastic, namely in cancerous tissues the IFP is far greater than in normal tissues. The reasons can be multiple: the absence of a well functioning lymphatic system in the tumour, an increased permeability of tumour vessels or the proliferation of tumour cells in a confined area [36]. Lastly, the chemotactic coefficient k_n is difficult to estimate. In fact, data on the chemotactic coefficient of glioma cells in response to oxygen concentration are not reported in literature, thus we refer to the order of magnitude found in [23] for bacterial chemotaxis in response to attractants, as amino acids and sugars.

3 Numerical model

In this section we describe the numerical scheme adopted to approximate numerically the system of partial differential equations (10) with patient-specific data. In particular, in subsection 3.1 we briefly describe the procedures to generate a patient-specific mesh and additional meshes containing the values of the independent components of the tensors $\mathbf{D}$ and $\mathbf{T}$, starting from MRI and DTI images. In subsection 3.2 we define the finite element approximation of (10), reporting the numerical algorithm to solve it. In the following, $[0, T]$ is the finite time interval in which we are considering the tumour evolving. The value of T will be specified in section 4 for each considered test case.

	Parameter description	Value	References
E	Brain Young modulus	694 Pa	[14]
ν	Tumour cells proliferation rate	0.012 – 0.5 day^{-1}	[45, 62]
ν_d	Tumour cells death rate	0.06 – 0.15 day^{-1}	[30]
M_{0h}	Healthy tissue inter-phase friction	1753.64 – 5032.2 (Pa day)/mm^2	[60]
M_0	Tumour inter-phase friction	1377.86 – 3991.06 (Pa day)/mm^2	[60]
ϕ_e	Equilibrium cell volume fraction	0.389	[9]
r	Tumour cell radius	0.005 – 0.01 mm	[65, 67]
χ_h	Healthy tissue interstitial fluid pressure	106.66 Pa	[7]
χ	Tumour interstitial fluid pressure	866.7 – 1533.3 Pa	[7]
ϵ	Diffuse interface thickness, $2r\sqrt{\chi}$	$0.29 - 0.78$ Pa$^{1/2}$mm	
k_n	Chemotactic coefficient	1296 mm^2/(mM day)	[23]
δ	Hypoxia threshold	0.15 – 0.5	[26, 30]
n_s	Oxygen concentration in vessels	0.07 mM	[67]
S_n	Oxygen supply rate	10^4 day^{-1}	[12]
D_n	Oxygen diffusion coefficient	86.4 mm^2/day	[45]
l_n	Oxygen penetration distance	0.1 mm	[26]
δ_n	Oxygen consumption rate, D_n/l_n^2	8640 day^{-1}	
m	Radiation fractions per day	1 day^{-1}	[58]
N_{days}	Total radiotherapy treatment days	30 day	[58]
N_d	Total radiation doses, nN_{days}	30	
d	Radiation dose	2 Gy	[58]
α	Linear coefficient for RT induced cell kill	0.027 Gy^{-1}	[50, 52]
α/β	Alpha-beta ratio	10 Gy	[24, 50, 53]
β	Quadratic coefficient for RT induced cell kill, $\alpha(\alpha/\beta)^{-1}$	0.0027 Gy^{-2}	
R_{eff}	Radiotherapy death rate, $\alpha md + \beta md^2$	0.0648 day^{-1}	
k_{C1}	Concomitant chemotherapy death rate	0.00735 day^{-1}	[50]
k_{C2}	First cycle of adjuvant CHT death rate	0.0147 day^{-1}	[50]
k_{C3}	Remaining cycles of adjuvant CHT death rate	0.0196 day^{-1}	[50]

Table 1: Values or ranges of values for parameters used in the models.

3.1 Mesh creation and preprocessing

We generate patient-specific computational meshes elaborating the actual clinical post-contrast T1-magnetic resonance images of a patient afflicted by GBM, kindly provided by *Istituto Neurologico Carlo Besta*. Starting from the greyscale MRI images, we create a computational mesh reproducing the shape of the patient's brain, conveniently refined in the area surrounding the tumour. Secondly, we generate several additional meshes: a labelled mesh carrying the information about the cerebral tissues position; six meshes representing the independent components of the symmetric diffusion tensor $\boldsymbol{D}$, describing water diffusion as given by the DTI images; six meshes associated with each independent component of the tensor of preferential directions $\boldsymbol{T}$, created from the components of $\boldsymbol{D}$ as explained below.

As oxygen is carried by the fluid component, the local values of tensor $\boldsymbol{D}$, which describes how nutrients diffuse effectively in a specific point of the brain, can be directly derived from DTI images. On the other hand, the tensor $\boldsymbol{T}$, representing the preferential movement directions of cells inside the brain, has the same eigenvectors of the tensor $\boldsymbol{D}$ but it is parameterised by a tuning parameter which enhances or reduces the anisotropy of DTI, as done in [37].

Namely, we set:

$$\hat{\boldsymbol{T}} = a_1(r)\lambda_1 \boldsymbol{e}_1 \otimes \boldsymbol{e}_1 + a_2(r)\lambda_2 \boldsymbol{e}_2 \otimes \boldsymbol{e}_2 + a_3(r)\lambda_3 \boldsymbol{e}_3 \otimes \boldsymbol{e}_3, \tag{14a}$$

$$\boldsymbol{T} = \frac{1}{\hat{T}_{av}}\hat{\boldsymbol{T}} = \frac{3}{tr(\hat{\boldsymbol{T}})}\hat{\boldsymbol{T}} = \frac{3}{a_1(r)\lambda_1 + a_2(r)\lambda_2 + a_3(r)\lambda_3}\hat{\boldsymbol{T}} \tag{14b}$$

where $\hat{T}_{av} = \frac{1}{3}tr(\hat{\boldsymbol{T}})$ is the mean diffusivity of $\hat{\boldsymbol{T}}$, characterizing the overall intensity of the diffusion process, λ_i and $\boldsymbol{e}_i$ for $i = 1, 2, 3$ are the descending ordered eigenvalues and the corresponding eigenvectors of $\boldsymbol{D}$ and $a_i(r)$ for $i = 1, 2, 3$ are functions of the anisotropy controlling factor r given by:

$$\begin{pmatrix} a_1(r) \\ a_2(r) \\ a_3(r) \end{pmatrix} = \begin{pmatrix} r & r & 1 \\ 1 & r & 1 \\ 1 & 1 & 1 \end{pmatrix} \begin{pmatrix} c_\ell \\ c_p \\ c_s \end{pmatrix} \tag{15}$$

In (15), c_ℓ, c_p and c_s are respectively the linear, planar and spherical anisotropy coefficients, defined as follows:

$$c_\ell = \frac{\lambda_1 - \lambda_2}{\lambda_1 + \lambda_2 + \lambda_3}, \qquad c_p = \frac{2(\lambda_2 - \lambda_3)}{\lambda_1 + \lambda_2 + \lambda_3}, \qquad c_s = \frac{3\lambda_3}{\lambda_1 + \lambda_2 + \lambda_3}. \tag{16}$$

By construction, $c_\ell + c_p + c_s = 1$. If $c_\ell \approx 1$ the diffusion is linear, along the main eigenvector $\boldsymbol{e}_1$; if $c_p \approx 1$, the diffusion is planar and confined within the plane generated by $\boldsymbol{e}_1$ and $\boldsymbol{e}_2$; lastly, if $c_s \approx 1$, we have isotropic, spherical diffusion. As a consequence of (14) and (15), when $c_\ell \approx 1$ only the eigenvalue along the main diffusion direction is multiplied by r, while in the planar case ($c_p \approx 1$) only the two largest eigenvalues are modified. The tensor is not changed when the diffusion is isotropic ($c_s \approx 1$). Therefore, the introduction of the functions $a_i(r)$ has the purpose of controlling the tensor anisotropy without changing its orientation. Moreover, in order to respect the constraint $tr(\boldsymbol{T}) = 3$, the tensor is multiplied by an appropriate scalar factor.

When r equals 1, i.e. when the anisotropy is not emphasized, the tensor is not changed, while $r < 1$ corresponds to a decrease in anisotropy and $r > 1$ to an increase in anisotropy. If $r = 1$ we have that $\hat{\boldsymbol{T}} = \boldsymbol{D}$ and the tensor $\boldsymbol{T} = \frac{1}{D_{av}}\boldsymbol{D}$ is reduced to a simple re–scaling of the diffusion tensor: the existence of a relationship between $\boldsymbol{D}$ and $\boldsymbol{T}$ is sustained by the fundamental hypothesis that the chemotactic movement of cells is similar to the diffusion of water measured by DTI since both of them follow the alignment of fibers. Indeed, it has been observed that glioma cells velocity on aligned fibers is five times greater than on randomly oriented fibers [38]. In the following simulations, we will set $r = 3$.

3.2 Finite Element discretization

In this section we introduce the finite element and time discretization of the system (10).

Let $\mathcal{T}_h$ be a quasi-uniform conforming decomposition of Ω into tetrahedra K, and let us introduce the following finite element spaces:

$$Q_h := \{\chi \in C(\bar{\Omega}) : \chi|_K \in \mathbb{P}^1(K)\ \forall K \in \mathcal{T}_h\} \subset H^1(\Omega),$$
$$Q_h^+ := \{\chi \in S^h : \chi \geq 0 \text{ in } \Omega\}$$

where $\mathbb{P}_1(K)$ indicates the space of polynomials of total order one on K.

Let J be the set of nodes of $\mathcal{T}_h$ and $\{\mathbf{x}_j\}_{j\in J}$ be the set of their coordinates. Moreover, let $\{\varphi_j\}_{j\in J}$ be the Lagrangian basis functions associated with each node $j \in J$. Denoting by $\pi^h : C(\bar{\Omega}) \to S^h$ the standard Lagrangian interpolation operator we define the lumped scalar product as

$$(\eta_1, \eta_2)^h = \int_\Omega \pi^h(\eta_1(\mathbf{x})\eta_2(\mathbf{x}))d\mathbf{x} \equiv \sum_{j\in J}(1, \chi_j)\eta_1(\mathbf{x}_j)\eta_2(\mathbf{x}_j), \tag{17}$$

for all $\eta_1, \eta_2 \in C(\bar{\Omega})$.

We set $\Delta t = T/N$ for a $N \in \mathbb{N}$ and $t_n = n\Delta t$, $n = 0, ..., N$. Starting from data $\phi_0, n_0 \in H^2(\Omega)$ and $\phi_h^0 = \pi^h \phi_0$, $n_h^0 = \pi^h n_0$, with $0 \leq \phi_h^0 < 1$, we consider the following fully discretized problem: for $n = 1, \dots, N$, given $(\phi_h^{n-1}, n_h^{n-1}) \in Q_h^+ \times Q_h^+$, find $(\phi_h^n, \Sigma_h^n, n_h^n) \in Q_h^+ \times Q_h \times Q_h^+$ such that, $\forall (v_h, w_h, q_h) \in Q_h \times Q_h^+ \times Q_h$,

$$\begin{aligned}\left(\frac{\phi_h^n - \phi_h^{n-1}}{\Delta t}, v_h\right)^h = &-\frac{1}{M_0}(\phi_h^{n-1}(1-\phi_h^{n-1})^2 \boldsymbol{T}\nabla\Sigma_h^n, \nabla v_h) + \nu(\phi_h^{n-1}[n_h^n - \delta]_+(1-\phi_h^{n-1}), v_h)^h \\ &- \nu_d(\phi_h^{n-1}[\delta - n_h^n]_+, v_h)^h + k_n n_s(\phi_h^{n-1}\boldsymbol{T}\nabla n_h^n, \nabla v_h) - ((k_R + k_C)\phi_h^{n-1}, v_h)^h,\end{aligned} \tag{18a}$$

$$\epsilon^2(\nabla\phi_h^n, \nabla(w_h - \phi_h^n)) + (\psi_1'(\phi_h^n), w_h - \phi_h^n)^h \geq (\Sigma_h^n - \psi_2'(\phi_h^{n-1}), w_h - \phi_h^n)^h, \tag{18b}$$

$$\left(\frac{n_h^n - n_h^{n-1}}{\Delta t}, q_h\right)^h = -(\boldsymbol{D}\nabla n_h^n, \nabla q_h) + S_n((1-n_h^n)(1-\phi_h^{n-1}), q_h)^h - \delta_n(\phi_h^{n-1} n_h^n, q_h)^h, \tag{18c}$$

where $(\cdot, \cdot)$ denotes the standard L^2 inner product over Ω, and the following convex splitting of the potential is considered:

$$\psi_1(\phi) = -E(1-\phi_e)\ln(1-\phi), \quad \psi_2(\phi) = -E\left[\frac{1}{3}\phi^3 + \frac{1-\phi_e}{2}\phi^2 + (1-\phi_e)\phi\right]. \tag{19}$$

In (18) equation (10a) is discretized starting from its dual mixed weak formulation, introducing the chemical potential variable Σ, defined in (8b).

The variational inequality (18b) enforces the positivity of the discrete solution since it implies that ϕ_h^n is projected onto the space with positive values Q_h^+. This projection aims at recovering the analytical properties of the continuous solution. Indeed, the solution of (10a) can be shown to satisfy a positivity constraint. Entropy estimates which guarantee the positivity of the continuous solution can be obtained by formally multiplying (10a) by $\log(\phi(\mathbf{x}, t))$, integrating on Ω_T and using Gronwall arguments. Since these estimates are not straightforwardly available at the discrete level, as $\log(\phi_h^n)$ is not available as test function in the space Q_h in (18), we impose this property as a constraint through a variational inequality. In particular, choosing $w_h \equiv 0$ and $w_h \equiv 2\phi_h^n$ in (18) yields, for all $j \in J$, that either $\phi_h^n(x_j) = 0$ or $\phi_h^n(x_j) > 0$ and $\epsilon^2(\nabla\phi_h^n, \nabla\phi_j) + (\psi_1'(\phi_h^n) + \psi_2'(\phi_h^{n-1}) - \Sigma_h^n, \phi_j)^h = 0$ (see [1] for details). Moreover, from Energy estimates it is possible to show that the logarithmic singularity of ψ_1 guarantees that $\phi_h^n < 1$ $\forall n$ if $\phi_h^0 < 1$.

The lumping approximation of the L^2 scalar product is introduced in (18) in order for the discrete solution to be able to track compactly supported solutions of (10) with a free boundary which moves with a finite speed of velocity, selecting the physical solutions with compact support and moving boundary from the ones with fixed support. The presence of these unphysical discrete solutions with fixed support is linked to the non-uniqueness of the solution of the degenerate Cahn-Hilliard equation, e.g. as described in [6]. Indeed, let us introduce a proper subdivision of J into a set of *passive nodes* $J_0(\phi_h^{n-1}) \subset J$ such that $(\phi_h^{n-1}, \varphi_j) = 0$ for $j \in J_0(\phi_h^{n-1})$ and a set of *active nodes* $J_+(\phi_h^{n-1}) = J \setminus J_0(\phi_h^{n-1})$. A passive node is thus characterized by the fact that $\phi_h^{n-1} \equiv 0$ on the support of the basis function associated to it. Choosing $v_h \equiv \varphi_i$, $i \in J_0(\phi_h^{n-1})$, in (18), and noting that the right hand side of the first equation of (18) is equal to zero, we get that the values of $\phi_h^n(\mathbf{x}_i)$, for each $i \in J_0(\phi_h^{n-1})$, are set to zero, leaving the values on the other nodes where $\phi_h^{n-1} = 0$ free to take non-zero values. This introduces the property of a moving support with finite speed for the discrete solution, since the support can expand at most of a length equal to h_K, the diameter of the tetrahedra to which the passive node belongs, at each time step.

In order to solve the system (18) for every time step n, we generalize the iterative procedure introduced in [5] and [1] and formulate the following algorithm:

Require: $\mu > 0$ (a relaxation parameter), $\phi_h^{n-1}, \Sigma_h^{n-1}$;
for $k \geq 0$ **do**
Initialization

$$\phi_h^{n,0} = \phi_h^{n-1}, \Sigma_h^{n,0} = \Sigma_h^{n-1};$$

Step 1 Find $z^{n,k} \in Q_h$ such that $\forall w_h \in Q_h$:

$$(z^{n,k}, w_h)^h = (\phi_h^{n,k}, w_h)^h - \mu[\epsilon^2(\nabla\phi_h^{n,k}, \nabla w_h) + (\psi_2'(\phi_h^{n-1}) - \Sigma_h^{n,k}, w_h)^h];$$

Step 2 Find $\phi_h^{n,k+1/2} \in Q_h^+$, $\forall r \geq 0$, such that:
if $j \in J_0(\phi_h^{n-1})$ **then**

$\phi_h^{n,k+1/2}(\mathbf{x}_j) \leftarrow \phi_h^{n-1}(\mathbf{x}_j)$

else

$$(\phi_h^{n,k+1/2}(\mathbf{x}_j) + \mu\psi_1'(\phi_h^{n,k+1/2})(\mathbf{x}_j) - z^{n,k}(\mathbf{x}_j), r - \phi_h^{n,k+1/2}(\mathbf{x}_j)) \geq 0 \tag{20}$$

end if

Step 3 Find $(\phi_h^{n,k+1}, \Sigma_h^{n,k+1}, n_h^n) \in Q_h \times Q_h \times Q_h$, $\forall (v_h, w_h, q_h) \in Q_h \times Q_h \times Q_h$, such that:

$$\begin{cases} \frac{1}{\Delta t}(\phi_h^{n,k+1}, v_h)^h + & \frac{1}{M_0}(\boldsymbol{T}\nabla\Sigma_h^{n,k+1}, \nabla v_h) - k_n n_s(\phi_h^{n-1}\boldsymbol{T}\nabla n_h^n, \nabla v_h) = \\ & \frac{1}{\Delta t}(\phi_h^{n-1}, v_h)^h + \nu(\phi_h^{n-1}[n_h^n - \delta]_+(1-\phi_h^{n-1}), v_h)^h - \nu_d(\phi_h^{n-1}[\delta - n_h^n]_+, v_h)^h + \\ & \left(\left[\frac{1-\phi_h^{n-1}(1-\phi_h^{n-1})^2}{M_0}\right]\boldsymbol{T}\nabla\Sigma_h^{n,k}, \nabla v_h\right) - ((k_R + k_C)\phi_h^{n-1}, v_h)^h, \\ (\phi_h^{n,k+1}, w_h)^h + & \mu\epsilon^2(\nabla\phi_h^{n,k+1}, \nabla w_h) - \mu(\Sigma_h^{n,k+1}, w_h)^h = (2\phi_h^{n,k+1/2} - z_h^{n,k} - \mu\psi_2'(\phi_h^{n-1}), w_h)^h, \\ \frac{1}{\Delta t}(n_h^n, q_h)^h + & (\boldsymbol{D}\nabla n_h^n, \nabla q_h) + S_n(n_h^n(1-\phi_h^{n-1}), q_h)^h + \delta_n(\phi_h^{n-1}n_h^n, q_h)^h = \\ & \frac{1}{\Delta t}(n_h^{n-1}, q_h)^h + S_n(1-\phi_h^{n-1}, q_h)^h. \end{cases}$$

if $||\phi_h^{n,K+1} - \phi_h^{n,K}||_\infty < 10^{-6}$ **then**

$(\phi_h^n, \Sigma_h^n, n_h^n) \leftarrow (\phi_h^{n,K+1}, \Sigma_h^{n,K+1}, n_h^n)$; **break**.

end if

end for

The variational inequality (20) contains the elliptic terms in the forcing term $z^{n,k}$ only, which is a known term at the step $k + 1/2$, and hence can be solved as a projection problem on each active node independently. In order to solve it, we solve the following projected gradient method in the index l, $l = 0, \ldots, L$, starting from $\phi_h^{n,k+1/2,0} = \phi_h^{n,k}$:

$$\phi_h^{n,k+1/2,l+1}(\mathbf{x}_j) = \max\left\{0, \phi_h^{n,k+1/2,l}(\mathbf{x}_j) - \omega[\phi_h^{n,k+1/2,l}(\mathbf{x}_j) + \mu\psi_1'(\phi_h^{n,k+1/2,l}(\mathbf{x}_j)) - z_h^{n,k}]\right\}, \tag{21}$$

where ω is a relaxation parameter. If $\|\phi_h^{n,k+1/2,L+1} - \phi_h^{n,k+1/2,L}\|_\infty < 10^{-6}$, we stop the cycle and set $\phi_h^{n,k+1/2} = \phi_h^{n,k+1/2,L+1}$. Note that, since the operator acting on $\phi_h^{n,k+1/2,l}$ in the square bracket in (21) is continuous and strictly monotone, the projection map defined in (21) has a unique fixed point [21].

4 Results

In this section we present the numerical results obtained solving the GBM growth model (10). The GBM evolution is simulated without therapies and with therapies after surgical removal. The patient-specific mesh obtained with the method presented in section 3 is adopted. The numerical algorithm is implemented by means of FEniCS [2], a computing platform for partial differential equations with high-level Python and C++ interfaces [43].

Throughout the computations we have introduced a numerical analogue of the set $J_0(\phi_h^{n-1})$ where $\phi_h^{n-1} < 10^{-6}$ is meant for $\phi_h^{n-1} = 0$. Furthermore, we implement an adaptive time step in order to avoid numerical errors associated to an excessively long time interval. Since the support of the discrete solution can move at most for a length h_K locally at each time step, where h_K is the diameter of a tetrahedra K which contains a passive node, the CFL-type condition $\Delta t < h_{min}/v_{max}$ must be guaranteed, being h_{min} the smallest edge length among the mesh cells and v_{max} the maximum on Ω of the infinity norm of the tumour expansion velocity, calculated as the phase velocity of the tumour cells in (1). Namely, we impose

$$\Delta t = \min\left(100 \cdot \frac{M_0}{E^2}\epsilon^2, \frac{h_{min}}{2v_{max}}\right) \tag{22}$$

where $M_0\epsilon^2/E^2$ is the typical time scale for the spinodal decomposition dynamics of ϕ [12]. The phase velocity of the tumour cells $\boldsymbol{V}$ is set to zero on the passive nodes and otherwise is calculated by considering both the chemotactic and the mechanical expansion of the tumour cells, i.e.

$$\boldsymbol{V} = k_n n_s \boldsymbol{T}\nabla n - \frac{(1-\phi)^2}{M_0}\boldsymbol{T}\nabla\Sigma\,. \tag{23}$$

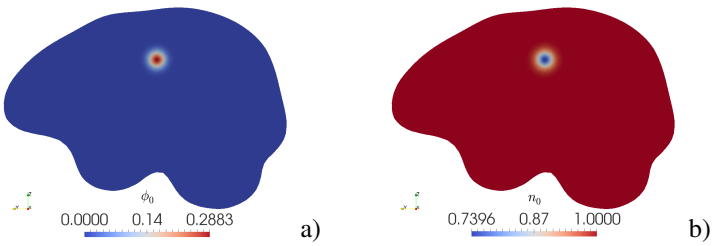

Figure 3: X-normal slices of the cancerous cell volume fraction ϕ (a) and nutrient n (b) at the initial time step.

Hence,

$$v_{max} := \max_{\mathbf{x}_j}(|V_x(\mathbf{x}_j)| + |V_y(\mathbf{x}_j)| + |V_z(\mathbf{x}_j)|), \tag{24}$$

being V_i the components of the velocity vector $\boldsymbol{V}$. Thereby, the expansion of the support of the solution is not blocked by the presence of passive nodes.

Throughout the simulations reported in the next subsections, the values of the following biological and numerical parameters, established on the basis of Table 1, are kept fixed: $E = 694$ Pa, $\nu = 0.08$ 1/day, $\nu_d = 0.04$ 1/day, $M_0 = 5000$ (Pa day)/mm^2, $\phi_e = 0.389$, $\epsilon = 0.35$ Pa$^{1/2}$mm, $\delta = 0.3$, $n_s = 0.07$ mM, $S_n = 10^4$ 1/day, $D_n = 86.4$ mm^2/day, $\delta_n = 8640$ 1/day, $k_n = 2$ mm^2/(mM day), $\mu = 0.0046875$ and $\omega = 0.0646$. The basic temporal step is $\Delta t = 100 \cdot M_0\epsilon^2/E^2 = 0.1225$ day, which is approximately equivalent to 3 hours.

4.1 Boundary and initial conditions in simulations

Since GBM has a high infiltrating nature, it does not exhibit a sharp interface at the tumour-host boundary, hence we assume that at the initial instant $t = 0$ the neoplastic volume fraction $\phi_0(\mathbf{x}) := \phi(\mathbf{x}, 0)$ follows a normal distribution in space, for suitable coefficients a and b:

$$\phi_0(\mathbf{x}) = ae^{-\frac{1}{b^2}(\mathbf{x}-\mathbf{x}_c)^2}. \tag{25}$$

In particular we choose $a = 0.3$ and $b^2 = 20$, $b \sim \sqrt{20}$ being the (conventional) radius of the tumour. The initial datum has thus a maximum, smaller than ϕ_e, located in the center $\mathbf{x}_c$ of the tumour (identified from the medical images) and decreases smoothly to zero (Fig. 3a). The initial oxygen distribution $n_0(\mathbf{x}) := n(\mathbf{x}, 0)$ is obtained by solving the steady version of the nutrient governing equation:

$$-\nabla \cdot (\boldsymbol{D}\nabla n_0) = S_n(1 - n_0)(1 - \phi_0) - \delta_n\phi_0 n_0\,, \tag{26}$$

where ϕ_0 is the initial cancerous cells distribution. Thus the oxygen distribution reflects the profile of ϕ_0: outside the tumour, where the tissue is healthy and ϕ_0 close to 0, the nutrient concentration is equal to 1, whereas it decreases to its minimum while approaching to the core of the tumour (Fig. 3b).

As the tumour can not grow beyond the cranial skull, we impose a homogeneous Neumann condition on the cell volume fraction and on the chemical potential, while a non homogeneous Dirichlet condition applies for the nutrient:

$$\nabla\phi \cdot \boldsymbol{n} = 0 \qquad \forall \mathbf{x} \in \partial\Omega\,, \tag{27a}$$

$$\nabla\Sigma \cdot \boldsymbol{n} = 0 \qquad \forall \mathbf{x} \in \partial\Omega\,, \tag{27b}$$

$$n = 1 \qquad \forall \mathbf{x} \in \partial\Omega \tag{27c}$$

where $\boldsymbol{n}$ is the outward boundary normal.

4.2 Effect of anisotropy and heterogeneity on GBM growth

To study the influence of anisotropy and heterogeneity on tumour evolution, we examine three different cases:

- *isotropic homogeneous* growth: the GBM grows inside an homogeneous and isotropic environment, i.e. $\boldsymbol{T} = \text{diag}(1, 1, 1)$ and $\boldsymbol{D} = D_n\boldsymbol{T}$;

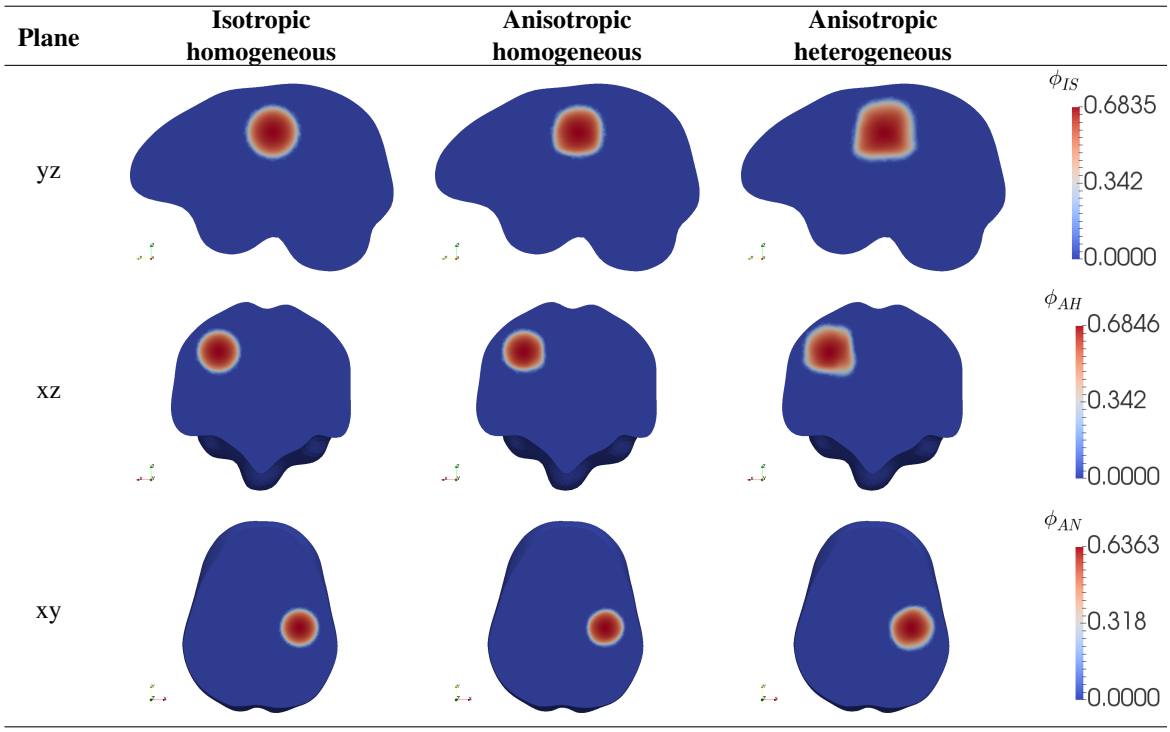

Figure 4: Comparison between the expansion of the tumour with isotropic (IS), homogeneous anisotropic (AH) and heterogeneous anisotropic (AN) diffusion, at $t = 180$ days, showing the mesh clipped along yz-plane (view from left), xz-plane (frontal view) and xy-plane (view from the top).

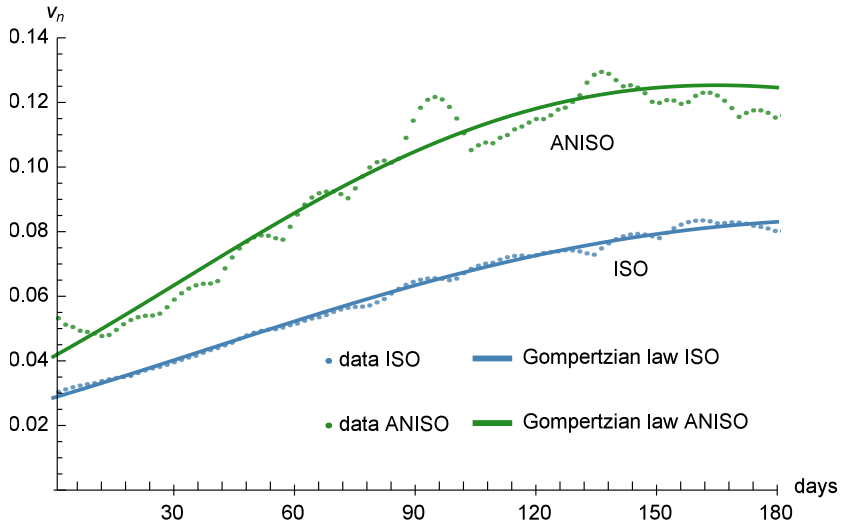

Figure 5: Maximum value of expansion velocity v_n of the tumour front over time, monitored in the isotropic homogeneous (ISO) and anisotropic heterogeneous (ANISO) simulations. The dots correspond to the numerical values of the front velocity recorded along the direction orthogonal to the tumour front, i.e. $v_n := \max_{\mathbf{x}_j} \boldsymbol{V} \cdot \boldsymbol{n}$, where $\boldsymbol{V}$ is defined in (23) and $\boldsymbol{n}$ is the direction orthogonal to the tumour front. The solid lines are the fitting of the numerical data with a Gompertz curve $v_n = rck \exp\big(-c \exp(-rt)\big) \exp(-rt)$, with $k = 15.3944 \pm 0.0916$, $c = 3.2626 \pm 0.0034$, $r = 0.0056 \pm 2.52\,\text{e-}5$ in the ISO case, and $k = 47.9809 \pm 0.3333$, $c = 3.3060 \pm 0.0116$, $r = 0.0071 \pm 4.76\,\text{e-}5$ in the ANISO case, calculated by a non-linear least-squares fitting method.

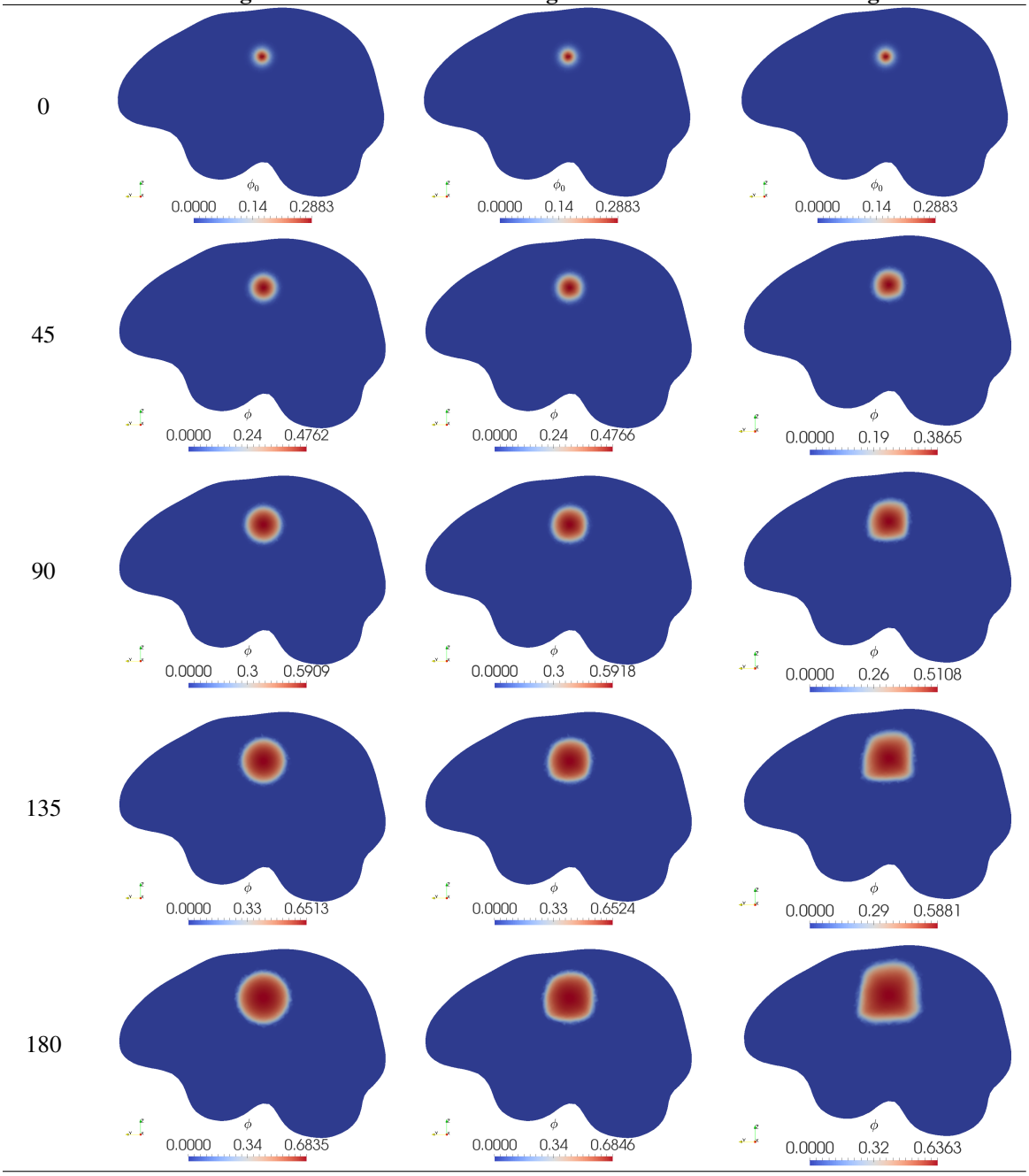

Figure 6: Stages of tumour evolution at t = 0, 45, 90, 135, 180 days considering isotropic, anisotropic homogeneous and anisotropic heterogeneous diffusion and the absence of therapies.

- *anisotropic homogeneous* growth: patient-specific anisotropic diffusion of nutrients and cell motion is considered, i.e., $\boldsymbol{D}$ and $\boldsymbol{T}$ are obtained from DTI images as explained in section 3.1, whereas the other model parameters are considered homogeneous inside the brain;

- *anisotropic heterogeneous* growth: using anisotropic $\boldsymbol{D}$ and $\boldsymbol{T}$ data, we choose the value of the chemotaxis parameter k_n to be four times the basic value inside the white matter, where cells can easily migrate along the fibers bundles. Thus, $k_n = 8$ mm^2/mM day in white matter and $k_n = 2$ mm^2/mM day in grey matter and cerebrospinal fluid.

The results of the simulations reporting GBM growth over a period of nearly six months are compared in Fig. 4. In the isotropic and homogeneous case, the tumour expands equally in all directions, preserving the initial spherical shape and nearly doubling its radius (Fig. 4, first column). When the actual anisotropic diffusion is considered, with chemotactic parameter k_n homogeneous, the tumour takes a more sharp-cornered shape, especially in yz- and xz-planes, whereas in the xy-plane the tumour section appears essentially equal to the isotropic case. The tumour size is comparable with the isotropic homogeneous simulation, the cell volume fraction reaching almost the same maximum value $\phi_{max} = 0.68$ (Fig. 4, second column). When considering an heterogeneous chemotactic coefficient k_n, the velocity of growth clearly increases and the tumour is located mainly in the white matter, where the value of k_n is higher. Therefore, the cell volume fraction ϕ expands more rapidly its support, while its maximum increases more slowly, with respect to the previous cases. We notice also that the shape is more notched and irregular, reflecting the same preferential directions in the yz and xz planes highlighted by the homogeneous anisotropic case (Fig. 4, third column).

In all cases, the maximum value of the expansion velocity of the tumour front follows a Gompertzian profile [41] (Fig. 5), reaching values in the same order of magnitude of the maximal expansion speed reported in the literature, i.e. 0.09 - 0.11 mm/day [38]. The maximum value of expansion velocity is calculated as $v_n := \max_{\mathbf{x}_j} \boldsymbol{V} \cdot \boldsymbol{n}$, where $\boldsymbol{V}$ is defined in (23) and $\boldsymbol{n}$ is the direction orthogonal to the tumour front. Observing the curves in Fig. 5 in the isotropic homogeneous case, we note a bouncing behaviour in the numerical data when the tumour expands beyond the refined sub–region of the mesh, which is a numerical effect due to the mesh structure. This behaviour is more pronounced in the anisotropic heterogeneous simulation, where it depends also on the anisotropy and the heterogeneity of the transport terms in the model.

In Fig. 6, we report different evolution stages for each simulation in order to compare how the tumour changes morphology during the growth. From left to right are shown the isotropic homogeneous case, the anisotropic homogeneous case and the anisotropic heterogeneous case. The tumour is depicted, from the top row, at $t = 0$, 45, 90, 135, 180 days. The maximum values of ϕ grow in time, with the highest value in the anisotropic homogeneous case and the lowest value in the anisotropic heterogeneous case, at each time step. The differences in shape are visible from the beginning, but become relevant at earlier stages.

The shape evolution recorded during the anisotropic GBM growth is strongly affected by the underlying fiber orientation, encoded in the tensor $\boldsymbol{T}$. In Fig. 7 is plotted the final pattern of ϕ superimposed onto the plots of the diagonal components of the tensor $\boldsymbol{T}$ along the xy, xz and yz planes. We observe that, in the yz-plane, the high value of T_{yy} in the lower region of the tumour causes an elongation in the y direction when the tumour is extended enough to reach this zone, whereas the high T_{zz} on the right-hand side of the tumour in the xz-plane creates a flattened border along the z direction. On the other hand, the almost isotropic expansion in the xy-plane reflects the moderate values of T_{xx} and T_{yy} in the surroundings of the tumour.

These results show how the growth of the tumour is greatly influenced by the diffusion tensor $\boldsymbol{D}$ and the tensor of preferential directions $\boldsymbol{T}$. The tumour location largely determines the shape generated during the evolution, as in the so-called *butterfly gliomas* [20], a particular type of GBM that extends through both the cerebral hemispheres via the *corpus callosum*, creating the image of a bilateral symmetric lesion resembling the wings of a butterfly. Indeed, the corpus callosum is the largest white matter structure inside the brain, located in its center, and formed by a thick bundle of aligned neural fibers connecting the two hemispheres so that they can communicate with each other. Within it, cells are forced to migrate in one specific direction, causing the tumour to spread into both the hemispheres and gets this particular shape. Even though the tumour considered in our simulations does not originate inside the corpus callosum, in accordance with medical data, from the first and second row of Fig. 7 it is clear that the presence of this anatomical structure attracts the tumour infiltration (i.e., the central red zone in the xz-plane of the T_{xx} map).

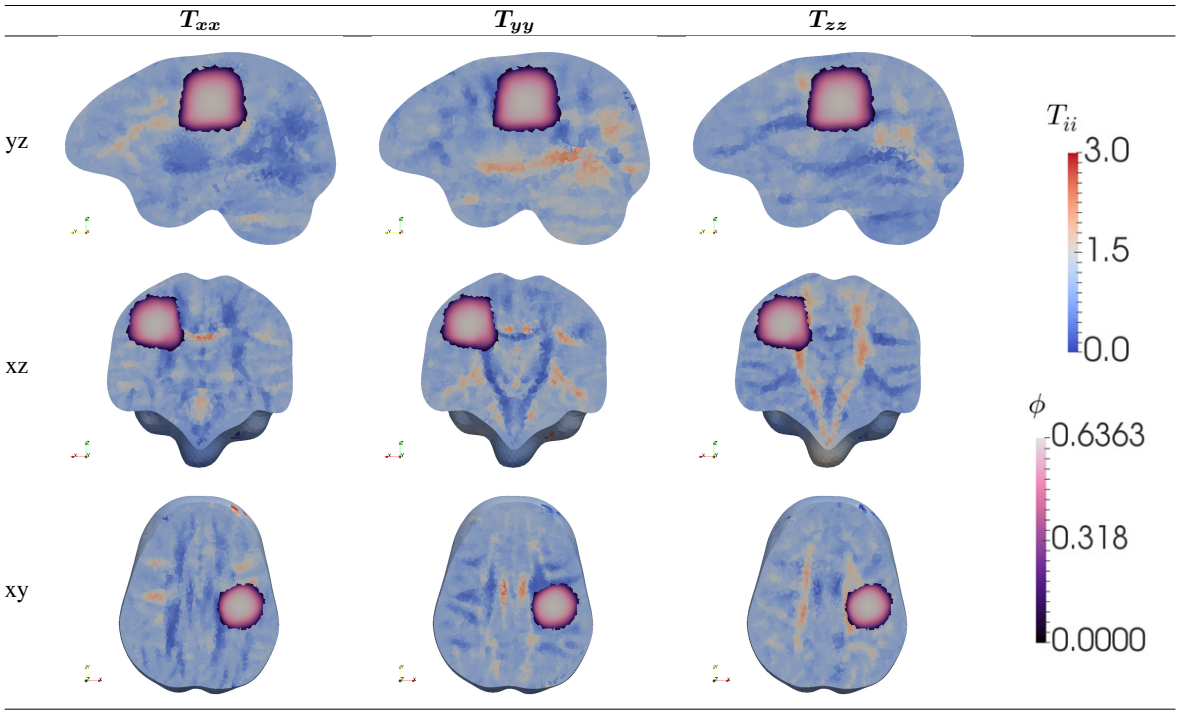

Figure 7: T_{xx}, T_{yy} and T_{zz} meshes cut along yz, xz and xy planes, with the anisotropic heterogeneous tumour at 180th day superimposed.

4.3 Effect of therapies on GBM regrowth after resection

Finally, we simulate a GBM treated with surgical resection, chemotherapy and radiotherapy, according to the standard Stupp protocol explained in section 2.2, by discretizing the system of equations (10). We assume that the removed region coincides with the tumour visible in the magnetic resonance images analysed in the Appendix. However, due to the very strong infiltrating attitude of glioblastoma, the removal of the whole cancerous mass is almost impossible, hence some neoplastic cells generally remain in the peritumoral area. After resection, the cavity is filled by fluid, forming an edema.

The incomplete removal of malignant cells is represented in the initial datum: small islands of neoplastic cells, with $\phi = 0.3$, surround the removed tumour. The computational meshes are modified accordingly to reproduce the edema inside the cavity (Fig. 8). The diffusion tensor in the cavity is given by the isotropic tensor $\boldsymbol{D} = d_m \text{diag}(1, 1, 1)$, being d_m the medium diffusion coefficient inside the fluid; then we change the heterogeneous parameter k_n accordingly and

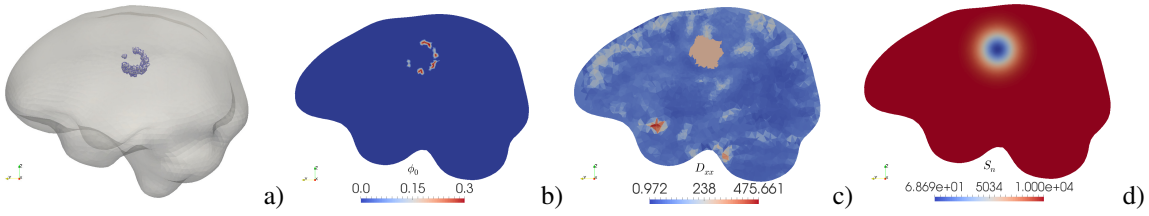

Figure 8: (a) Initial datum for therapy simulations, i.e. small islands of neoplastic cells surrounding the resected tumour; (b) x-normal slice of the cancerous cell volume fraction ϕ at the initial time step, after tumour resection; (c) values of D_{xx} after tumour resection; (d) nutrient source parameter S_n replicating the absence of vasculature inside the cavity.

assign the parameter S_n a normal profile going from zero in the center of the cavity up to its former value 10^4 1/day in healthy tissue, in order to replicate the absence of vasculature inside the removed region.

We run four types of heterogeneous anisotropic simulations considering the following conditions:

- *no therapy*: neither chemotherapy nor radiotherapy are administered after resection;
- *standard therapy*: after resection, the remaining tumour mass is treated accordingly to the standard Stupp protocol;
- *increased CHT*: the cytotoxic effect on cancer cells of the chemotherapeutic agent is boosted, maintaining the same cycles of administration of the Stupp protocol;
- *increased RT*: the sensitivity of the brain tissue to radiotherapy is enhanced, while keeping the chemotherapy dose and cycles of administration scheduled by the Stupp protocol.

The evolution of the tumour mass, for the four considered cases, is reported in Fig. 9 at $t = 42$, 75, 103, 131, 159, 187 days, which correspond to the end of every cycle of chemotherapy (when simulated).

Firstly, we observe the evolution of the islands of cancerous cells when neither chemotherapy nor radiotherapy are administered (first column of Fig. 9). The islands become increasingly broader in time until blending into a whole mass, which expands following the same preferential paths of the previous anisotropic heterogeneous simulation. After 187 days, the tumour mass has almost reached the brain border. We remark that, at the center of the cancerous mass, cells remain separated, forming a hole, since there the source term for the nutrient vanishes. Moreover, although the maximum of ϕ constantly grows, it reaches a lower value than the corresponding anisotropic heterogeneous simulation. Let us notice that the island appearing and growing in the top-left corner of the tumour is due to a little group of neoplastic cells already present in the initial datum, which is however not visible on the mesh clipped along the yz-plane (cf. Fig. 8a).

Afterwards, we simulate the tumour treatment according to the standard Stupp protocol, by using the model (10) and the parameters reported in Table 1. As shown in Fig. 9 (second column), for the set of parameters considered, the standard Stupp protocol is ineffective in stopping the tumour evolution. Indeed, the tumour islets become broader and ultimately blend into a single one, assuming a shape analogous to the simulation in absence of treatment. However, in this case, the cancer front velocity and the maximum tumour cell volume fraction ϕ_{max} at each time step are lower than in the simulation without therapy.

Therefore, we present two hypothetical variations of the standard therapeutic treatment, boosting chemotherapy and radiotherapy separately: in the increased CHT case, we raise ten-fold the effect of the daily doses of chemotherapy, setting $k_{C1} = 0.0735$ 1/day, $k_{C2} = 0.147$ 1/day and $k_{C3} = 0.196$ 1/day, whereas in the increased RT case we choose a ten-fold higher sensitivity of the tissue to radiotherapy, namely $\alpha = 0.27$ Gy^{-1}. The evolution steps are shown in the second and third columns of Fig. 9, respectively. In both cases the GBM expansion is greatly reduced in comparison with the standard therapeutic schedule. Particularly, while CHT alone does not prevent tumour regrowth, the boost in sensitivity to radiotherapy leads to complete regression of the tumour: at the end of the RT treatment ϕ_{max} reaches a minimum value that can be approximated by zero. This result is in accordance with clinical evidences [66] that have demonstrated a statistically significant survival benefit from postoperative radiotherapy compared with different chemotherapy schedules without radiation. The efficacy of chemotherapy in treating brain tumours is hampered by the presence of the blood-brain barrier, which notably reduces the dose of drug that actually reaches the tumour region, and by the non-responsiveness to chemotherapy of some types of cancer. Indeed, GBM is traditionally considered very refractory to chemotherapy and post-operative external beam radiotherapy has been the standard treatment for GBM until, in the late 1990s, the addition of TMZ to radiotherapy was proved to add some benefits to radiotherapy alone [58, 59, 66].

It is interesting to notice that the trend of ϕ_{max} during each treatment is not monotonic (cf. Fig. 10). Indeed the tumour strongly regresses during the radiotherapy administration period, specifically during the 5-days cycles, assuming a nearly exponential profile. After radiotherapy, the tumour resumes to grow, experiencing decrease only during the chemotherapy administration weeks. In Fig. 10 we report the values of ϕ_{max} for each considered therapeutic treatment, at the beginning and at the end of every RT or CHT cycle. We notice that the previously mentioned oscillatory behaviour is evident in all the simulations besides the last one, in which the tumour is essentially eradicated after the cycle of radiotherapy with concurrent chemotherapy.

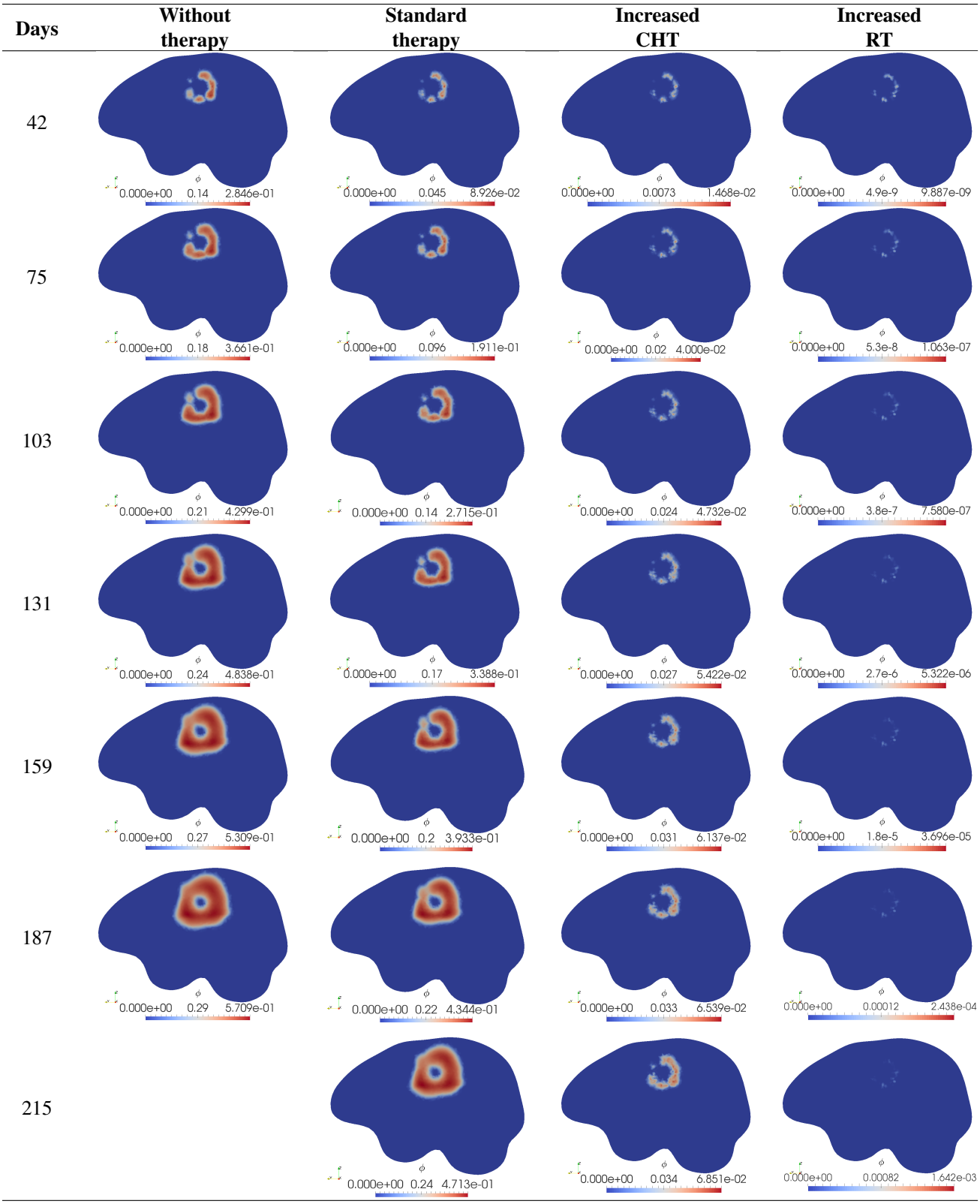

Figure 9: Stages of anisotropic heterogeneous tumour evolution at t = 42, 75, 103, 131, 159, 187, 215 days with no therapy and three different therapeutic schemes: standard Stupp protocol, a ten-fold higher CHT dose and a ten-fold higher sensitivity to RT.

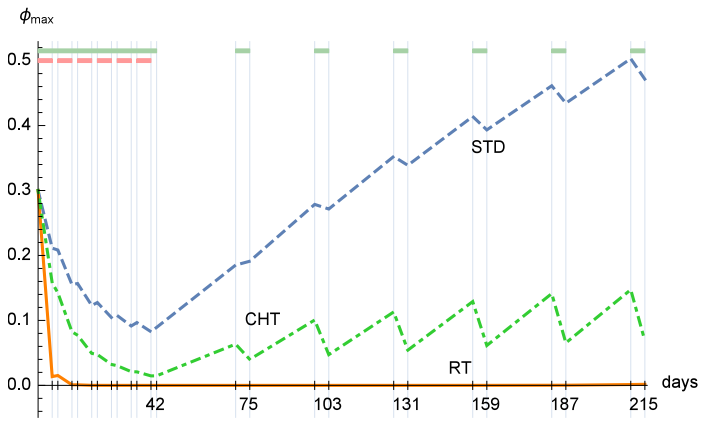

Figure 10: The curves show the values of ϕ_{max} at t = 0, 5, 7, 12, 14, 19, 21, 26, 28, 33, 35, 40, 42, 70, 75, 98, 103, 126, 131, 154, 159, 182, 187, 210, 215 days, i.e. at the beginning and at the end of each RT and CHT administration period (highlighted in the topmost part of the graphic with red and green rectangles, respectively), for the three analysed therapeutic schemes: standard therapy (STD, blue dashed line), higher CHT dose (green dot-dashed line) and higher sensitivity to RT (continuous orange line).

5 Discussion and conclusion

In this work we have illustrated a continuous mechanical model and a computational tool for reproducing the personalised GBM growth and progression after resection and therapies. The diffuse–interface model consists in a degenerate Cahn-Hilliard equation with single-well potential for the cancer cells volume fraction, coupled with a reaction diffusion equation for the nutrient. The effects of therapies, such as chemotherapy and radiotherapy, have been included in the model in order to predict the progression of the disease after the standard clinical protocol.

Due to the complexity of the proposed model, we also developed a stable numerical algorithm to discretize the system of equations, selecting the physical meaningful solution and enforcing the positivity constraint, generalizing recently developed algorithms proposed for the degenerate Cahn-Hilliard equation [5] [1]. The numerical code has been implemented by using the finite element method for a patient-specific 3D geometry, reconstructed from MRI clinical data, in order to simulate the spatio-temporal evolution of the cancerous mass inside the brain. Moreover, we included in the model the heterogeneity and the anisotropy of the brain fiber bundles, directly obtained from the neuroimaging DTI data on the same patient.

This approach represents a remarkable advancement with respect to the state-of-the-art GBM models. Indeed, the proposed model takes into account not only biochemical factors, such as nutrients availability and the chemotactic motion of cells, but also mechanical interactions occurring between the local micro-environment and the tumour, which play a fundamental role in cancer progression and invasion. Another point of strength of this computational model is the ability of support clinical strategies in a virtual environment using patient-specific data, mainly through the insertion of the tensor of preferential directions $\boldsymbol{T}$, which make the cells movements dependent on the brain architecture of each patient. In particular, in the case of a free growing GBM, the comparison between the fully anisotropic heterogeneous simulation and the isotropic homogeneous one suggests that the integration of DTI data in the model is of fundamental importance in order to reproduce patient-specific tumour evolution. In addition, the expansion velocity of the tumour front has the same order of magnitude of the one reported in clinical studies.

Finally, the model can be used to reproduce both the clinically-relevant case of GBM recurrence after incomplete surgical resection, where a group of cancerous cells is left into the peritumoral area, and the effect of subsequent cycles of radiotherapy and chemotherapy treatments. In particular, resection and therapies have been simulated according to the standard Stupp protocol, which seems to have limited efficacy in preventing GBM regrowth in the numerical simulations. A sensitivity analysis of the results for a single therapeutic action has been performed. The simulations have highlighted a high sensitivity to radiotherapy, displaying a strong regression with the increase of the radiation dose.

The results presented in this work can be evaluated as a proof–of–concept, a further step towards the ambitious goal to provide a computational tool that support medical doctors in clinical practice in a patient-specific manner. Nonetheless, these results need to be quantitatively validated by comparing the predicted evolution with the real progression of the disease inside the patient brain, directly measured from neuro–imaging data. Future developments of the model should investigate the role of mechanical stress exerted by the healthy brain on the growing GBM, e.g. by considering more complex mechanical constitutive equations of the cancer cell phase. Finally, one should consider a heterogeneous, time–dependent source term for nutrients, as blood vessels lie mostly in grey matter and can be dynamically formed by tumour-induced angiogenesis.

In conclusion, this work represents one more step towards the definition of a computational tool combining clinical data with a mathematical model that is able to capture both chemical and mechanical phenomena driving GBM evolution. This multidisciplinary approach has the potential to aid clinicians in the definition of therapeutic strategies in personalised oncology.

Acknowledgments

The neuroimaging data used in this study are gently provided by Francesco Acerbi and Alberto Bizzi (Istituto Neurologico Carlo Besta, Milan, Italy). We are indebted to Aymeric Stamm (Politecnico di Milano) and Elena Faggiano (University of Pavia) for their valuable collaboration in the development of the procedures for MRI and DTI image analysis and mesh creation.

This work is funded by AIRC MFAG grant 17412 and by *INdAM–GNFM* (National Group of Mathematical Physics) through the program *Progetto Giovani 2017*.

References

[1] A. Agosti, P. F. Antonietti, P. Ciarletta, M. Grasselli, and M. Verani, A Cahn-Hilliard type equation with application to tumor growth dynamics, Math. Meth. Appl. Sci., (2017). DOI: 10.1002/mma.4548.

[2] M. S. Alnaes, J. Blechta, J. Hake, A. Johansson, B. Kehlet, A. Logg, C. Richardson, J. Ring, M. E. Rognes, and G. N. Wells, The FEniCS Project Version 1.5, Archive of Numerical Software **3** (2015).

[3] D. Ambrosi and L. Preziosi, On the closure of mass balance models for tumor growth, Math. Models Methods Appl. Sci. **12(5)**, 737-754 (2002).

[4] L. Antiga, M. Piccinelli, L. Botti, B. Ene-Iordache, A. Remuzzi, and D. A. Steinman, An image-based modeling framework for patient-specific computational hemodynamics, Med. Biol. Eng. Comput. **46**, 1097-1112 (2008).

[5] J. W. Barrett, J. F. Blowey, and H. Garcke, Finite Element Approximation of the Cahn-Hilliard Equation with Degenerate Mobility, SIAM J. Numer. Anal. **37(1)**, 286-318 (1999).

[6] F. Bernis and A. Friedman, Higher order nonlinear degenerate parabolic equations, J. Differ. Equ. **83**, 179-206 (1990).

[7] Y. Boucher, H. Salehi, B. Witwer, G. R. Harsh, and R. K. Jain, Interstitial fluid pressure in intracranial tumours in patients and in rodents, Br. J. Cancer **75(6)**, 829-836 (1997).

[8] R. M. Bowen, Theory of mixtures, in: Continuum Physics, vol. 3, edited by A.C. Eringen (Academic Press, New York, 1976), Part I.

[9] M. Bruehlmeier, U. Roelcke, P. Bläuenstein, J. Missimer, P. A. Schubiger, J. Th. Locher, R. Pellikka, and S. M. Ametamey, Measurement of the Extracellular Space in Brain Tumors Using ^{76}Br-Bromide and PET, J. Nucl. Med. **44(8)**, 1210-1218 (2003).

[10] P. K. Burgess, P. M. Kulesa, J. D. Murray, and E.C. Alvord Jr, The interaction of growth rates and diffusion coefficients in a three-dimensional mathematical model of gliomas, J. Neuropathol. Exp. Neurol. **56**, 704-713 (1997).

[11] H. Byrne and L. Preziosi, Modelling solid tumour growth using the theory of mixtures, Math. Med. Biol. **20**, 341-366 (2003).

[12] C. Chatelain, T. Balois, P. Ciarletta, and M. Ben Amar, Emergence of microstructural patterns in skin cancer: a phase separation analysis in a binary mixture, New J. Phys. **13(11)**,115013-115033 (2011).

[13] L. L. Chen, S. Ulmer, and T. S. Deisboeck, An agent-based model identifies MRI regions of probable tumor invasion in a patient with glioblastoma, Phys. Med. Biol. **55(2)**, 329-338 (2010).

[14] O. Clatz, M. Sermesant, P. Bondiau, H. Delingette, S. K. Warfield, G. Malandain, and N. Ayache, Realistic Simulation of the 3D Growth of Brain Tumors in MR Images Coupling Diffusion with Biomechanical Deformation, IEEE Trans. Med. Imaging **24(10)**, 1334-1346 (2005).

[15] M.C. Colombo, C. Giverso, E. Faggiano, C. Boffano, F. Acerbi, and P. Ciarletta, Towards the Personalized Treatment of Glioblastoma: Integrating Patient-Specific Clinical Data in a Continuous Mechanical Model, PLoS ONE **10(7)**, e0132887 (2015).

[16] V. Cristini, H. B. Frieboes, X. Li, J. S. Lowengrub, P. Macklin, S. Sanga, S. M. Wise, and X. Zheng, Nonlinear Modeling and Simulation of Tumor Growth, Selected Topics in Cancer Modeling, 113-182 (2008).

[17] V. Cristini, X. Li, J. S. Lowengrub, and S. M. Wise, Nonlinear simulations of solid tumor growth using a mixture model: invasion and branching, J. Math. Biol. **58**, 723-763 (2009).

[18] T. Deisboeck, M. Berens, A. Kansal, S. Torquato, A. Stemmer-Rachamimov, and E. Chiocca, Pattern of self organization in tumour systems: complex growth dynamics in a novel brain tumour spheroid model, Cell Prolif. **34(2)**, 115-134 (2001).

[19] M. Doi and A. Onuki, Dynamic coupling between stress and composition in polymer solutions and blends, Journal de Physique II **2(8)**, 1631-1656 (1992).

[20] K. Dziurzynski, D Blas-Boria, D. Suki, D. P. Cahill, S. S. Prabhu, V. Puduvalli, and N. Levine, Butterfly glioblastomas: a retrospective review and qualitative assessment of outcomes, J. Neuro Oncol. **109(3)**, 555-563 (2012).

[21] I. Ekeland and R. Temam, Convex analysis and variational problems (SIAM, 1999).

[22] C. Engwer, T. Hillen, M. Knappitsch, and C. Surulescu, Glioma follow white matter tracts: a multiscale DTI-based model, J. Math. Biol. **71(3)**, 551-582 (2015).

[23] R. M. Ford and D. A. Lauffenburger, Analysis of chemotactic bacterial distributions in population migration assays using a mathematical model applicable to steep or shallow attractant gradients, Bull. Math. Biol. **53(5)**, 721-749 (1991).

[24] J. F. Fowler, The linear-quadratic formula and progress in fractionated radiotherapy, Br. J. Radiol. **62**, 679-694 (1989).

[25] H. B. Frieboes, F. Jin, Y. Chuang, S. M. Wise, J. S. Lowengrub, and V. Cristini, Three-dimensional multispecies nonlinear tumor growth-II: Tumor invasion and angiogenesis, J. Theor. Biol. **264**, 1254-1278 (2010).

[26] H. B. Frieboes, J. S. Lowengrub, S. Wise, X. Zheng, P. Macklin, E. L. Bearer, and V. Cristini, Computer simulation of glioma growth and morphology, NeuroImage **37**, S59-S70 (2007).

[27] H. B. Frieboes, X. Zheng, C.H. Sun, B. Tromberg, R. Gatenby, and V. Cristini, An Integrated Computational/-Experimental Model of Tumor Invasion, Cancer Res. **66(3)**, 1597-1604 (2006).

[28] F. B. Furnari, T. Fenton, R. M. Bachoo, A. Mukasa, J. M. Stommel, A. Stegh, W. C. Hahn, K. L. Ligon, D. N. Louis, C. Brennan, L. Chin, R. A. DePinho, and W. K. Cavenee, Malignant astrocytic glioma: genetics, biology, and paths to treatment, Genes Dev. **21**, 2683-2710 (2007).

[29] H. Garcke, K. F. Lam, E. Sitka, and V. Styles, A Cahn-Hilliard-Darcy model for tumour growth with chemotaxis and active transport, Math. Models Methods Appl. Sci. **26(6)**, 1095-1148 (2016).

[30] P. Gerlee and A. R. A. Anderson, An Evolutionary Hybrid Cellular Automaton Model of Solid Tumour Growth, J. Theor. Biol. **246(4)**, 583-603 (2007).

[31] A. Giese, R. Bjerkvig, M. E. Berens, and M. Westphal, Cost of migration: invasion of malignant gliomas and implications for treatment, J. Clin. Oncol. **21(8)**, 1624-1636 (2003).

[32] M. L. Goodenberger and R. B. Jenkins, Genetics of adult glioma, Cancer Genet. **205**, 613-621 (2012).

[33] H. L. P. Harpold, E. C. Alvord Jr, and K. R. Swanson, The Evolution of Mathematical Modeling of Glioma Proliferation and Invasion, J. Neuropath. Exp. Neurol. **66(1)**, 1-9 (2007).

[34] H. Hatzikirou, A. Deutsch, C. Schaller, M. Simon, and K. Swanson, Mathematical modelling of glioblastoma tumour development: a review, Math. Models Methods Appl. Sci. **15(11)**, 1779-1794 (2005).

[35] A. Hawkins-Daarud, K. G. van der Zee, and J. T. Oden, Numerical simulation of a thermodynamically consistent four-species tumor growth model, Int. J. Numer. Methods Biomed. Eng. **28**, 3-24 (2012).

[36] R. K. Jain, Transport of Molecules in the Tumor Interstitium: A Review, Cancer Res. **47**, 3039-3051 (1987).

[37] S. Jbabdi, E. Mandonnet, H. Duffau, L. Capelle, K. R. Swanson, M. Pelegrini-Issac, R. Guillevin, and H. Benali, Simulation of Anisotropic Growth of Low-Grade Gliomas Using Diffusion Tensor Imaging, Magn. Reson. Med. **54**, 616-624 (2005).

[38] J. Johnson, M. O. Nowicki, C. H. Lee, E. A. Chiocca, M. S. Viapiano, S. E. Lawler, and J. J. Lannutti, Quantitative Analysis of Complex Glioma Cell Migration on Electrospun Polycaprolactone Using Time-Lapse Microscopy, Tissue Eng. Part C **15 (4)**, 531-540 (2009).

[39] A. R. Kansal, S. Torquato, G. R. Harsh, E. A. Chiocca, and T. S. Deisboeck, Simulated Brain Tumor Growth Dynamics Using a Three-Dimensional Cellular Automaton, J. Theor. Biol. **203(4)**, 367-382 (2000).

[40] L. J. Kaufman, C. P. Brangwynne, K.E. Kasza, E. Filippidi, V. D. Gordon, T. S. Deisboeck, and D. A. Weitz, Glioma expansion in collagen I matrices: analyzing collagen concentration-dependent growth and motility patterns, Biophys. J. **89(1)**, 635-650 (2005).

[41] A. K. Laird, Dynamics of tumor growth, Br. J. Cancer **18(3)**, 490-502 (1964).

[42] D. Le Bihan, J. F. Mangin, C. Poupon, C. A. Clark, S. Pappata, N. Molko, and H. Chabriat, Diffusion tensor imaging: concepts and applications, J. Magn. Reson. Im. **13**, 534-546 (2001).

[43] A. Logg and G. N. Wells, DOLFIN: Automated Finite Element Computing, ACM Trans. Math. Softw. **37** (2010).

[44] P. Macklin and J. S. Lowengrub, A New Ghost Cell/Level Set Method for Moving Boundary Problems: Application to Tumor Growth, J. Sci. Comput. **35**, 266-299 (2008).

[45] A. Martinez-Gonzalez, G. F. Calvo, L. A. Perez, and V. M. Perez-Garcia, Hypoxic Cell Waves Around Necrotic Cores in Glioblastoma: A Biomathematical Model and Its Therapeutic Implications, Bull. Math. Biol. **74(12)**, 2875-2896 (2012).

[46] S. F. C. O'Rourke, H. McAneney, and T. Hillen, Linear quadratic and tumour control probability modelling in external beam radiotherapy, J. Math. Biol. **58**, 799-817 (2009).

[47] Q. T. Ostrom, H. Gittleman, J. Fulop, M. Liu, R. Blanda, C. Kromer, Y. Wolinsky, C. Kruchko, and J. S. Barnholtz-Sloan, CBTRUS Statistical Report: Primary Brain and Central Nervous System Tumors Diagnosed in the United States in 2008-2012, Neuro Oncol. **17**, iv1-iv62 (2015).

[48] K. J. Painter and T. Hillen, Mathematical modelling of glioma growth: The use of Diffusion Tensor Imaging (DTI) data to predict the anisotropic pathways of cancer invasion, J. Theor. Biol. **323**, 25-39 (2013).

[49] S. Pieper, M. Halle, and R. Kikinis, 3D SLICER, Proceedings of the 1st IEEE International Symposium on Biomedical Imaging: From Nano to Macro **1**, 632-635 (2004).

[50] G. Powathil, M. Kohandel, S. Sivaloganathan, A. Oza, and M. Milosevic, Mathematical modeling of brain tumors: effects of radiotherapy and chemotherapy, Phys. Med. Biol. **52**, 3291-3306 (2007).

[51] M. Preusser, H. Heinzl, E. Gelpi, K. Schonegger, C. Haberler, P. Birner, C. Marosi, M. Hegi, T. Gorlia, and J. A. Hainfellner, Histopathologic Assessment of Hot-Spot Microvessel Density and Vascular Patterns in Glioblastoma: Poor Observer Agreement Limits Clinical Utility as Prognostic Factors, Cancer **107**, 162-170 (2006).

[52] R. Rockne, E. C. Alvord Jr, J. K. Rockhill, and K. R. Swanson, A mathematical model for brain tumor response to radiation therapy, J. Math. Biol. **58**, 561-578 (2009).

[53] R. Rockne, J. K. Rockhill, M. Mrugala, A. M. Spence, I. Kalet, K. Hendrickson, A. Lai, T. Cloughesy, E. C. Alvord Jr, and K. R. Swanson, Predicting the efficacy of radiotherapy in individual glioblastoma patients in vivo: a mathematical modeling approach, Phys. Med. Biol. **55**, 3271-3285 (2010).

[54] R. K. Sachs, L. R. Hlatky, and P. Hahnfeldt, Simple ODE Models of Tumor Growth and Anti-Angiogenic or Radiation Treatment, Math. Comput. Model. **33**, 1297-1305 (2001).

[55] A. C. Shieh, Biomechanical forces shape the tumor microenvironment, Ann. Biomed. Eng. **39(5)**, 1379-1389 (2011).

[56] H. Si, TetGen, a Delaunay-Based Quality Tetrahedral Mesh Generator, ACM Trans. Math. Softw. **41(2)**, 11:1-11:36 (2015).

[57] A. Stamm, O. Commowick, S. K. Warfield, and S. Vantini, Comprehensive Maximum Likelihood Estimation of Diffusion Compartment Models Towards Reliable Mapping of Brain Microstructure, MICCAI 2016, Athens, Greece, Part III (Springer, 2016), 622-630.

[58] R. Stupp et al., Radiotherapy plus Concomitant and Adjuvant Temozolomide for Glioblastoma, N. Engl. J. Med. **352**, 987-996 (2005).

[59] R. Stupp, M. Gander, S. Leyvraz and E. Newlands, Current and future developments in the use of temozolomide for the treatment of brain tumours, Lancet Oncol. **2**, 552-560 (2001).

[60] E. A. Swabb, J. Wei, and P. M. Gullino, Diffusion and Convection in Normal and Neoplastic Tissues, Cancer Res. **34**, 2814-2822 (1974).

[61] A. Swan, T. Hillen, J. Bowman, and A. Murtha, A Patient-Specific Anisotropic Diffusion Model for Brain Tumour Spread, Bull. Math. Biol. (2017).

[62] K. R. Swanson, E. C. Alvord Jr, and J. D. Murray, A quantitative model for differential motility of gliomas in grey and white matter, Cell Prolif. **33**, 317-329 (2000).

[63] K. R. Swanson, C. Bridge, J. D. Murray, and E. C. Alvord Jr, Virtual and real brain tumors: using mathematical modeling to quantify glioma growth and invasion, J. Neurol. Sci. **216**, 1-10 (2003).

[64] M. D. Szeto, G. Chakraborty, J. Hadley, R. Rockne, M. Muzi, E. C. Alvord Jr, K. A. Krohn, A. M. Spence, and K. R. Swanson, Quantitative metrics of net proliferation and invasion link biological aggressiveness assessed by MRI with hypoxia assessed by FMISO-PET in newly diagnosed glioblastomas, Cancer Res. **69(10)**, 4502-4509 (2009).

[65] M. L. Tanaka, W. Debinski, and I. K. Puri, Hybrid mathematical model of glioma progression, Cell Prolif. **42(5)**, 637-646 (2009).

[66] S. Villà, C. Balañà, and S. Comas, Radiation and concomitant chemotherapy for patients with glioblastoma multiforme, Chin. J. Cancer **33(1)**, 25-31 (2014).

[67] F. G. Vital-Lopez, A. Armaou, M. Hutnik, and C. D. Maranas, Modeling the Effect of Chemotaxis on Glioblastoma Tumor Progression, AIChE J. **57(3)**, 778-792 (2011).

[68] J. Z. Wang, Z. Huang, S. S. Lo, W. T. C. Yuh, and N. A. Mayr, A Generalized Linear-Quadratic Model for Radiosurgery, Stereotactic Body Radiation Therapy, and High-Dose Rate Brachytherapy, Sci. Transl. Med. **2(39)**, 39ra48 (2010).

[69] S. M. Wise, J. S. Lowengrub, H. B. Frieboes, and V. Cristini, Three-dimensional multispecies nonlinear tumor growth I - Model and numerical method, J. Theor. Biol. **253**, 524-543 (2008).

[70] J. Zhang, P. C. M. van Zijl, J. Laterra, A. Salhotra, B. Lal, S. Mori, and J. Zhou, Unique Patterns of Diffusion Directionality in Rat Brain Tumors Revealed by High-Resolution Diffusion Tensor MRI, Magn. Reson. Med. **58**, 454-462 (2007).

[71] `www.vtk.org`.

MOX Technical Reports, last issues

Dipartimento di Matematica
Politecnico di Milano, Via Bonardi 9 - 20133 Milano (Italy)

54/2017 Dede', L; Quarteroni, A.
Isogeometric Analysis of a Phase Field Model for Darcy Flows with Discontinuous Data

53/2017 Bertagna, L.; Deparis, S.;Formaggia, L.; Forti, D.; Veneziani A.
The LifeV library: engineering mathematics beyond the proof of concept

50/2017 Formaggia, F.; Vergara, C.
Defective boundary conditions for PDEs with applications in haemodynamics

51/2017 Gerbi, A.; Dede', L.; Quarteroni, A.
A monolithic algorithm for the simulation of cardiac electromechanics in the human left ventricle

52/2017 Beretta, E.; Ratti, L.; Verani, M.
A phase-field approach for the interface reconstruction in a nonlinear elliptic problem arising from cardiac electrophysiology

49/2017 Antonietti, P. F.,; Pennesi, G.
V-cycle multigrid algorithms for discontinuous Galerkin methods on non-nested polytopic meshes

48/2017 Regazzoni, F.; Dedè, L.; Quarteroni, A.
Active contraction of cardiac cells: a model for sarcomere dynamics with cooperative interactions

47/2017 Menghini, F.; Dede, L.; Forti, D.; Quarteroni, A.
Hemodynamics in a left atrium based on a Variational Multiscale-LES numerical model

46/2017 Agosti, A.; Gower, A.L.; Ciarletta, P.
The constitutive relations of initially stressed incompressible Mooney-Rivlin materials

45/2017 Gasperoni, F.; Ieva, F.; Paganoni, A.M.; Jackson C.H.; Sharples L.D.
Nonparametric frailty Cox models for hierarchical time-to-event data